IDENTIFICATION OF EARTHQUAKE INPUT EXCITATIONS FOR CSMIP-INSTRUMENTED BUILDINGS

S. F. Ghahari, and E. Taciroglu

Department of Civil & Environmental Engineering
University of California, Los Angeles

Abstract

This paper presents the results of a study on the identification of earthquake input excitations for CSMIP-Instrumented buildings. The true earthquake input motions exciting buildings may not be available for various reasons. For example, when there is Soil-Structure Interaction (SSI) effects, the recorded signal at the foundation level, which is commonly used as input excitation, is a part of the building's response. Also, the waves scattered from a vibrating building can alter the wave field around the building, so the so-called recorded Free-Field Motions (FFMs), another input motion candidate, could be polluted with these reflecting waves. Moreover, if there is significant Kinematic SSI, what actually a building experiences as input excitation is different from FFM and foundation response. These unmeasured motions are called Foundation Input Motions (FIMs) and have to be identified from recorded building's responses. In this paper, we propose various methods to carry out this task along with their verification, validation and real-life applications.

Introduction

Consideration of input excitations is an important ingredient of seismic design and assessment of building structures under earthquake hazards. Ground motions recorded on the ground surface—i.e., Free-Field Motions (FFMs)—have often been used as input excitations in seismic response analyses of structures. Such recordings are sometimes not true FFMs, in that they are polluted by waves scattered from nearby structures (see, e.g., [1]). More problematically, even the true FFMs are inherently different from what the subject structure experiences due to spatial variability as well as kinematic interaction effects (see, e.g., [2]). The other common option in dynamic analyses is to use the motion recorded at the foundation level as the input excitation. However, if there is an inertial interaction between the structure and the surrounding soil, the signal recorded at the foundation is part of the system's response [3], [4]. Such Soil-Structure Interaction (SSI) effects generally prevent the direct measurement of true input excitations. These true input excications are often referred to as Foundation input Motions (FIMs) [5]. The FIMs cannot be physically recorded unless there is a massless foundation without any building superstructure. **Figure 1** summarizes the aforementioned issues regarding the usage of various types recordings as earthquake input excitations. It is worth noting that even in the absence of SSI, for many real-life cases, the foundation responses are either at low Signal-to-Noise Ratio (SNR) levels or not recorded at all [6].

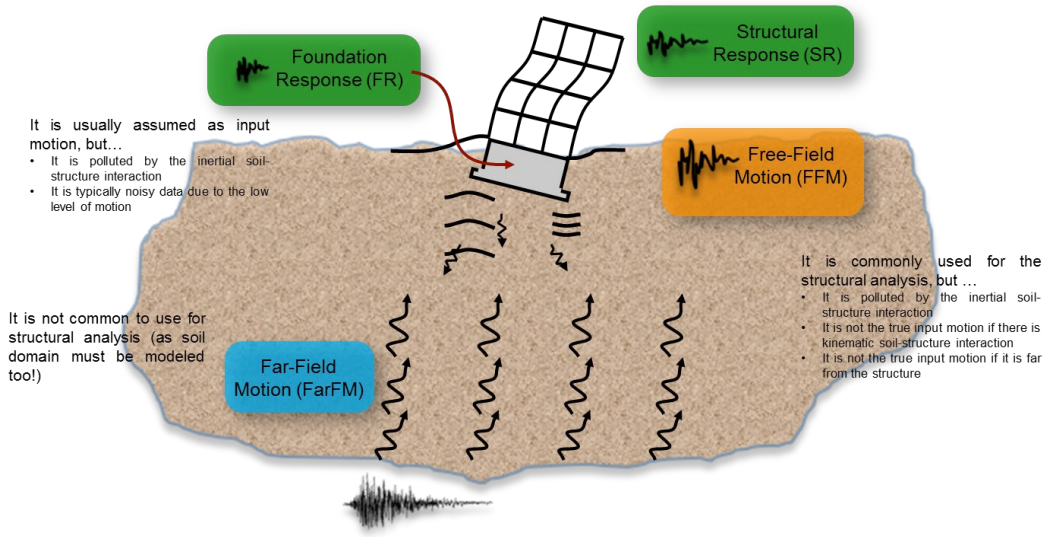

Figure 1. Available recording during an earthquake.

The back-calculation of FIMs from real-life data is a key capability for capturing actual earthquake input excitations and for validating new or existing procedures for considering SSI effects. The California Strong Motion Instrumentation Program (CSMIP) was established by California Geological Survey, in collaboration with various other agencies such as USGS and Caltrans in 1972 following the destructive 1971 San Fernando earthquake to obtain vital earthquake data for the engineering and scientific communities through a statewide network of strong motion instruments [7]. Through CSMIP, more than 900 stations were installed, including 650 ground-response stations, 170 buildings, 20 dams, and 60 bridges. A recent survey (**Table 1**) by the authors indicates that, at the present time, there are ~236 buildings with available instrumentation layouts and at least one earthquake dataset in the Center for Engineering Strong Motion Data (CESMD) [8]. The ~70% of the buildings are instrumented and maintained by the California Geological Survey (CGS) (**Figure 2**a) and this building inventory features various structural types as shown in **Figure 2**b.

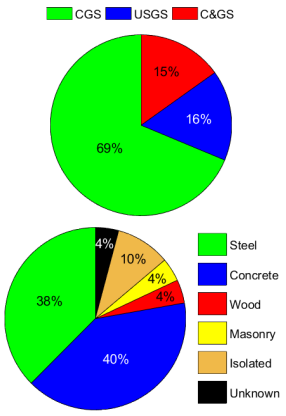

Figure 2. Distribution of CSMIP-instrumented buildings

Table 1. Available building data in CESMD.

Item Description	Number
Number of total records	1643
Number of buildings	377
Number of earthquakes	254
Number of earthquake sets	1588
Number of buildings with at least one earthquake	322
Number of buildings with at least one available earthquake	314
Number of buildings with the available layout	272
Number of buildings with the available layout and at least one recorded earthquake	243
Number of buildings with the available layout and at least one available earthquake	236

Identification Methods

The response of a building structure to a base excitation can be written as a time convolution as $x(t) = FIM(t) * h(t)$ where $FIM(t)$ and $h(t)$ are FIM signal and building's Impulse Response Function (IRF), respectively, and $*$ denotes time convolution. According to this relationship, an obvious way to recover FIM is through the deconvolution provided that building's IRF is known, while this is not the case for real problems because buildings are complex and unknown systems. Note that even having a building's IRF, the deconvolution process is a challenging task because the inverse of the IRF could (and mostly will) be an unstable filter which will be discussed later (see, e.g., [9]).

In a real-world scenario, the building is itself unknown and must be identified first or along with the FIMs. One way is to estimate the system (i.e., building's IRF) via numerical modeling. Despite the existing knowledge and tools for numerical modeling of structural systems, there are various sources of uncertainties (SSI, damping, non-structural, connections, etc.), which makes accurate modeling highly difficult even for very simple structures. Therefore, the building has to be identified. The simplest approach to identify building structures is through Operational Modal Analysis (OMA) for which large number of techniques have been developed in last few decades [10]–[14]. Yet, it is well accepted that the behavior of a structure during an earthquake would be different from its behavior under operational conditions. Also, the ambient data might be unavailable because the measurement system usually needs higher resolution and sensitivity. On the other hand, the identification of buildings using data recorded during strong seismic events without direct measurments of input excitations is challenging. This particular situation—namely, outout-only identification under strong excitations—has been a main focus of the authors in last decade.

The authors have developed a series of Blind[1] Modal Identification (BMID) methods for the aforementioned type of problems [15]–[21]. However, these methods nominally need dense instrumentation. Also, the level of uncertainty is not quantified because they are deterministic solutions. Another workaround is to use model-based solutions in which a numerical model with unknown parameter is assumed for the building under study. This model can be a simple Timoshenko beam as used by the authors [22]–[25] or a coupled beam used by Lignos and Miranda [6]. The problem with such solution is the potentially high level of modeling uncertainties that are not quantified in the mentioned studies. Recently, a series of output-only Bayesian Finite Element (FE) model updating methods have been proposed (see, e.g., [26]). In the present study, we used this method to estimate FIMs from real-life data recorded at the Millikan Library building [27]. While the results are promising, the computational cost is huge. to resolve this limiting fact, we developed a new series of solutions based on the Cross-Relation (CR) idea [28], [29]. The major idea behind this solution is to use response of several adjacent buildings that experience same excitation and extract input motion as common part. After presenting results of the Bayesian estimation of the Millikan Library, details of the proposed CR methods will be presented. A series of verification, validation, and application studies were

[1] Output-only

conducted by using these new solutions which are presented in this paper. To see a summary of the available FIM identification solutions discussed above **Figure 3** is presented.

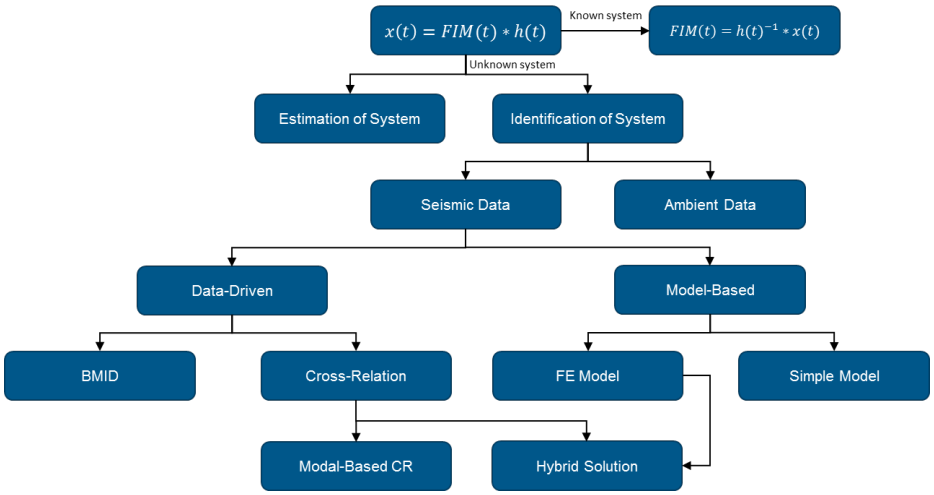

Figure 3. Available/developed solutions for FIM identification.

Output-Only Bayesian Estimation

The overall procedure of the output-only Bayesian estimation method is shown in **Figure 4** [30]. In this method, we assume a prior normal distribution for the unknown parameter vector **ψ** (collection of FE model's uncertain parameters and inputs) and propagate this uncertainty through the FE model. Based on the Bayes' rule, the posterior distribution is obtained by calculating the difference between the prediction and measurement (collected through sensors). This process sequentially continues in time. The details of the method are presented in Appendix A.

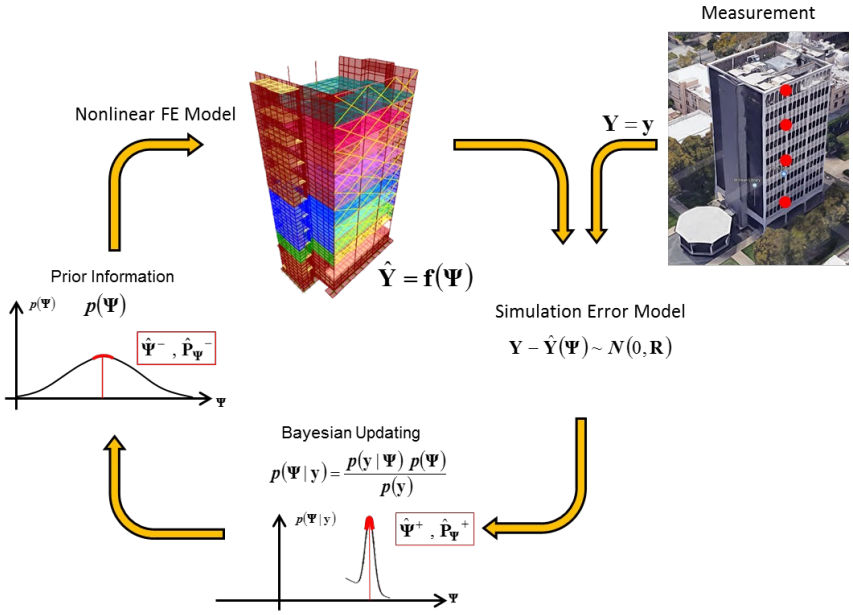

Figure 4. The output-only Bayesian estimation.

The method is already verified in various publications [31]. Herein, the method is used to estimate parameters of the FE model of the Millikan Library (**Figure 5**left) as well as unmeasured FIMs using real-life response signals during the 2002 Yorba Linda earthquake [27]. Using the available structural drawings, a detailed FE model of the structural system is developed [21]. We used the graphic-user-interface of SAP2000 software [32] to develop the initial geometry of the model. The SAP2000 model was then transferred to OpenSees [33]. The model uses linear-elastic beam-column elements to model beams and columns, and quadrilateral shell elements with linear-elastic section to model shear walls and slabs. The kinematic interaction of precast claddings installed on the north and south faces of the building with the structural system is modeled using diagonal brace elements. The damping energy dissipation for the time history analysis is defined using mass- and stiffness-proportional Rayleigh damping. The Rayleigh damping parameters are treated as unknowns to be estimated. The 3D model of the superstructure is shown in **Figure 5**right. Different colors in this figure present different material properties.

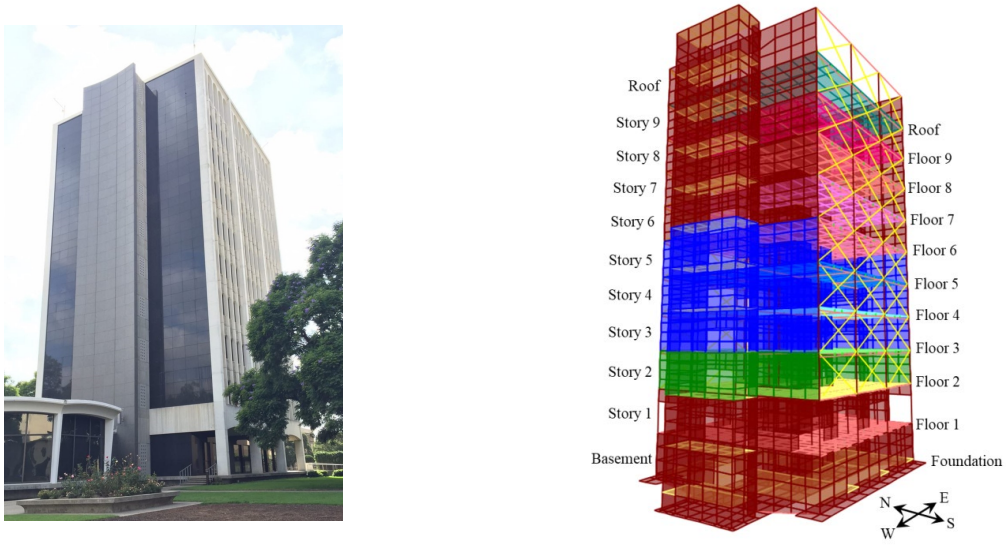

Figure 5. Developed the FE model of the Millikan Library structure.

To include SSI effects, distributed linear soil springs and dashpots are added underneath the foundation slab of the FE model as shown in **Figure 6**. As seen, the building has a two-level foundation system consisting of a central pad and two north and south foundation strips. Six unknown stiffness parameters, namely $k_x, k_{y1}, k_{y2}, k_{z1}, k_{z2}, k_{z3}$ are defined for different foundation regions. Likewise, six (unknown) parameters, namely $c_x, c_{y1}, c_{y2}, c_{z1}, c_{z2}, c_{z3}$, are used to define the damping.

The Bayesian estimation is carried out in two steps: In the first step, the foundation-level motions are used as uniform base input excitations to estimate the model parameters characterizing the structural model regardless of the soil subsystem. In this step, the torsional and rocking components of the foundation-level motion are also assumed as unknown input motions and estimated jointly with structural model parameters. In the second step, the identified structural model parameters are fixed at their mean estimates obtained from the first step, and the

three translational components of the FIM and parameters characterizing the soil-structure model and overall Rayleigh damping are estimated jointly. The second step comprises an output-only FE model updating.

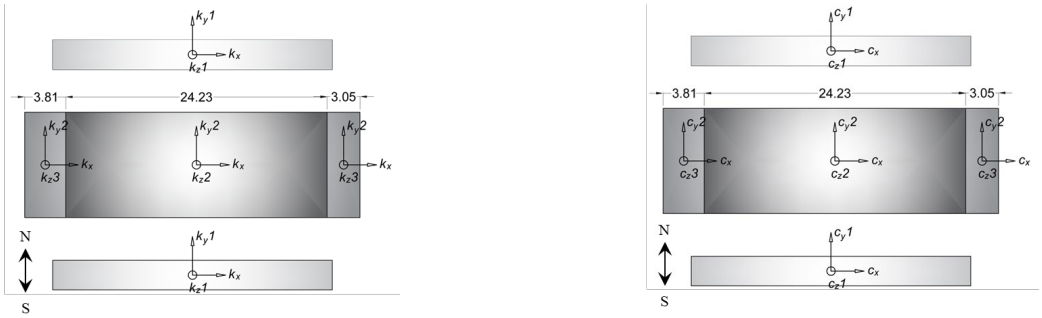

Figure 6. Foundation plan of the Millikan Library with six unknown subgrade stiffness (left) and damping (right) parameters.

Table 2 shows the initial and final estimate of the six model parameters along with their final estimated coefficient of variation (COV) at the end of the first step. The small values of the COVs denote that the identified values are reliable.

Table 2. Initial and final estimates of the model parameters along with the estimated coefficient of variation (COV).

Parameter ID	Description	Initial	Estimated	COV
1	Elastic modulus of brace elements (E_{Clad})	20 GPa	16.7 GPa	2.6%
2	Effective Elastic modulus of column/wall concrete at basement and 1st story ($E_{W\&C1}$)	17.3 GPa	33.6 GPa	1.0%
3	Effective Elastic modulus of column/wall concrete at 2nd story to Roof ($E_{W\&C2}$)	17.3 GPa	23.9 GPa	0.8%
4	Mass-proportional Rayleigh damping coefficient (a)	0.4	0.36	4.1%
5	Stiffness-proportional Rayleigh damping coefficient (b)	5.3×10^{-3}	1.4×10^{-3}	1.9%
6	Distributed floor mass on 1st to Roof floors (m)	250 kg/m^2	278.5 kg/m^2	2.0%

In the second step, we fix above mentioned six parameters in their identified values and identify 12 soil subsystem's parameters, the elastic modulus of the foundation (E_{Found}), and three translational FIMs. However, the identifiability study showed that not all 12 parameters are identifiable by using available instrumentation layout and stiffness and damping parameters in x and y directions must be reduced to one [27]. Also, a new set of Rayleigh damping parameters are identified, as those parameters identified in the first step represent a fixed-base system. The identified parameters of the soil subsystem are shown in **Table 3**. To evaluate how well the updated model prediction matches the measurement records, **Figure 7** compares the measured acceleration response time histories at the selected measurement channels with those estimated using the final estimates of the model parameters and FIMs. This figure shows a remarkable match between the estimated and measured acceleration responses.

Finally, **Figure 8** shows the time history of the posterior mean and standard deviation (SD) of the three components of the FIM.

Table 3. Initial and final estimates of the soil-structure parameters along with estimated COVs. Stiffness and damping parameters are in MN/m^3 and KNs/m^3, respectively, and E_{Found} is in GPa.

	k_x	k_{y1}	k_{z1}	k_{z2}	k_{z3}	c_x	c_{y1}	c_{z1}	a	b	E_{Found}
Initial	65	40	20	22.5	37.5	700	700	1000	0.36	1.4×10^{-3}	7.5
Estimated	158.7	73.4	139.0	93.5	111.9	685	1748	4126	0.01	1.0×10^{-3}	32.5
COV	5.4%	4.4%	1.0%	4.1%	2.9%	16.8%	3.3%	1.2%	55.4%	3.3%	3.6%

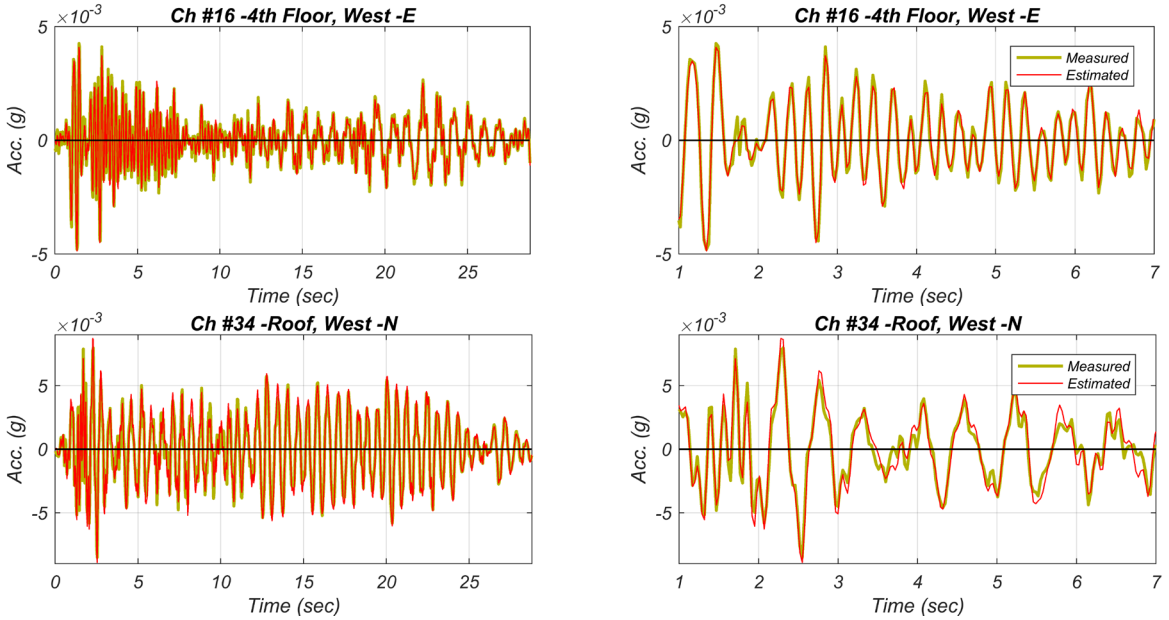

Figure 7. Comparison of the measured predicted responses. The right-hand-side plots magnify the response time history between 1-7 sec.

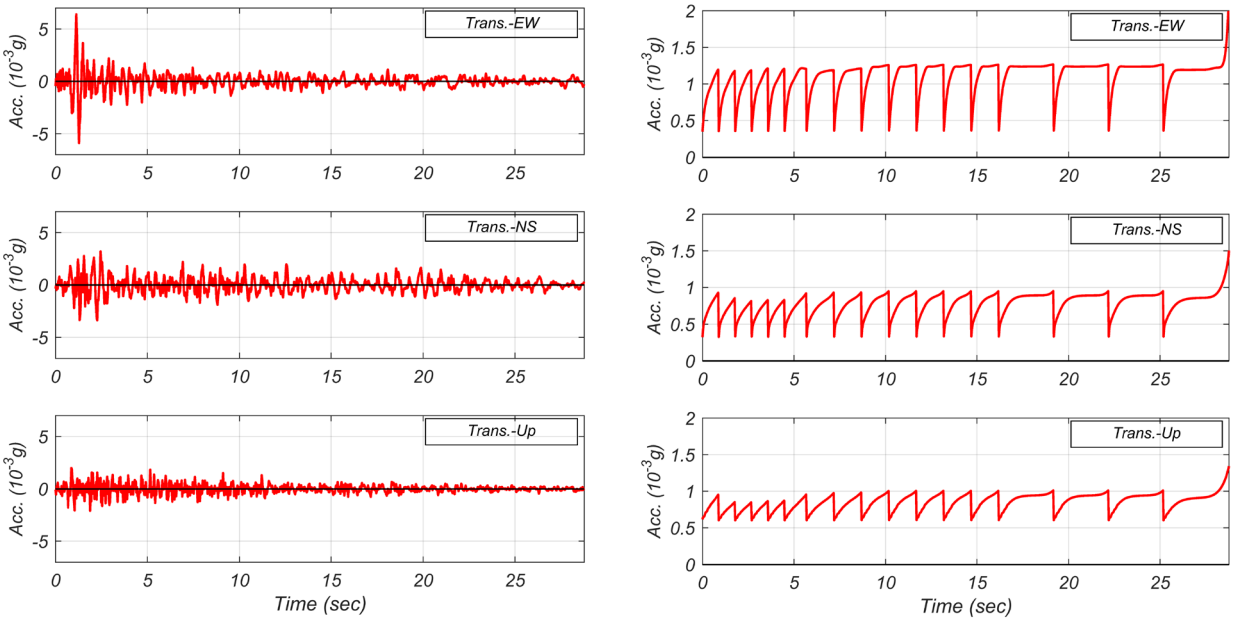

Figure 8. Estimated FIMs (left) and their standard deviation (right).

Cross-Relation Method

The model-based method presented in the previous section works very well and provides us with promising results along with the estimation uncertainties. However, it needs an initial numerical model free from modeling uncertainty, which may not available. Also, the method needs relatively dense instrumentation, and more importantly it is computationally very demanding because each time sample of the input motions is treated as an uncertain parameter. The authors have recently proposed a data-driven solution ([28], [29]) for site effect identification which works based on the Cross-Relation (CR) idea [34]. The method can be adopted to solve the present output-only system identification and FIM estimation as follows.

Assume that two adjacent buildings are excited under a similar input acceleration $\boldsymbol{s}$. The response of Buildings 1 and 2 can be written as a linear convolution of this input motion and each building's IRF as

$$\boldsymbol{x}_1 \cong \boldsymbol{h}_1 * \boldsymbol{s} \tag{1}$$

$$\boldsymbol{x}_2 \cong \boldsymbol{h}_2 * \boldsymbol{s} \tag{2}$$

where $\boldsymbol{h}_1$ and $\boldsymbol{h}_2$ are buildings' IRFs, respectively. Convolving both sides of Eqs. (1) and (2) by $\boldsymbol{h}_2$ and $\boldsymbol{h}_1$, respectively, we have

$$\boldsymbol{x}_1 * \boldsymbol{h}_2 - \boldsymbol{x}_2 * \boldsymbol{h}_1 = 0 \tag{3}$$

As seen, the equation above is a system of N equations (N is the total number of samples) with at most $2L$ unknown where L is the length of the longer IRF. So, provided that $N \geq 2L$, IRFs can be theoretically estimated. Once IRFs are estimated, unknown FIM can be backcalculated through the deconvolution.

The CR solution is simple and practical for CSMIP instrumented buildings, as our survey shows that even by imposing limiting criteria like distance less than 1 km (see, e.g., [35]) and similarity of the soil types, there are 29 and 23 candidate sets in Southern and Northern California, respectively, as shown in **Figure 9**.

Figure 9. Potential candidate sets for CR application in Southern (left) and Northern California (right).

While the CR method seems doable, there are some major challenges. The length of the IRFs for typical structures is not short which makes the estimation problem severely ill-conditioned. Also, the length is not a priori known. The CR method work based on the assumption that systems (here buildings) are dissimilar. So, if there is any similarity between these two adjacent buildings cannot be identified. Specifically, systems are unidentifiable at common zeros. To show this, let's assume that z-Transform [36] of IRFs can be factorized as $H_1(z) = (z - z_0)\bar{H}_1(z)$ and $H_2(z) = (z - z_0)\bar{H}_2(z)$. Then, Eq. (3) can be written as

$$X_1(z)(z - z_0)\bar{H}_2(z) - X_2(z) * (z - z_0)\bar{H}_1(z) = 0 \tag{4}$$

Obviously, systems are not identifiable at the common zero z_0. This issue is a critical issue when we notice that the length of IRFs is long and zeros of random polynomials cluster uniformly near the unit circles [37], which means lots of common zeros. In addition to these major problems, some minor issues like measurement noise, input excitation spatial variability, number of adjacent buildings, etc. must be addressed. In what follows, we propose various versions of the CR method whose applications depend on the complexity of the problem and the needed accuracy and reliability.

CR Method using Rational Transfer functions

Adding independent white Gaussian measurement noises $\boldsymbol{\nu}_1$ and $\boldsymbol{\nu}_2$ to Eqs. (1) and (2), Eq. (3) is rewritten as

$$\boldsymbol{x}_i * \boldsymbol{h}_j - \boldsymbol{x}_j * \boldsymbol{h}_i = \tilde{\boldsymbol{\nu}}_{ij} \tag{5}$$

where we used indices i and j, respectively, instead of 1 and 2 to be able to extend the solution to many buildings as will be discussed later. Also, $\tilde{\boldsymbol{\nu}}_{ij} = \boldsymbol{h}_j * \boldsymbol{\nu}_i - \boldsymbol{h}_i * \boldsymbol{\nu}_j$. Linear discrete-time convolution of Eq. (5) can be converted to multiplication by using the z-Transform as in

$$X_i(z^{-1})\, H_j(z^{-1}) - X_j(z^{-1})\, H_i(z^{-1}) = V_{ij}(z^{-1}) \tag{6}$$

In Eq. (6), H_i and H_j are z-Transforms of IRFs and are referred to as Transfer Functions (TFs) or System Functions [38], while X_i, X_j, and V_{ij} are the z-Transforms of $\boldsymbol{x}_i$, $\boldsymbol{x}_j$, and $\tilde{\boldsymbol{\nu}}_{ij}$, respectively. Theoretically, the IRFs have infinite length, but they can be recast as Infinite Impulse Response (IIR) filters by representing their corresponding TFs in the format of the ratio of complex polynomials

$$H(z^{-1}) = \frac{b_0 + b_1 z^{-1} + \cdots + b_{n_b} z^{-n_b}}{1 + a_1 z^{-1} + \cdots + a_{n_a} z^{-n_a}} \tag{7}$$

where the numerator $N(z^{-1}) = b_0 + b_1 z^{-1} + \cdots + b_{n_b} z^{-n_b}$ is an n_b-order polynomial with $n_b + 1$ parameters b_k $(k = 0, \ldots, n_b)$ representing a Moving Average (MA) part, and the denominator $D(z^{-1}) = 1 + a_1 z^{-1} + \cdots + a_{n_a} z^{-n_a}$ is an n_a-order polynomial with n_a parameters a_k $(k = 1, \ldots, n_a)$ representing an Autoregressive (AR) part. As seen, while the IRFs in their original MA form are infinitely long, their IIR representations have a finite length in both the numerator and the denominator. Using Eq. (7), the CR defined in Eq. (6) can be expressed as

$$X_i\, N_j D_i - X_j\, N_i D_j = V_{ij}\, D_i D_j, \tag{8}$$

where we dropped (z^{-1}) for simplicity. Eq. (8) can be further restated in a simplified form as

$$X_i\, G_{ij} - X_{\mathrm{j}}\, G_{ji} = E_{i,j} \tag{9}$$

where $G_{ij} = N_j D_i$ and $G_{ji} = N_i D_j$ are two Finite Impulse Response (FIR) filters with orders $n_{b_j} + n_{a_i}$ and $n_{a_j} + n_{b_i}$, respectively, and $E_{i,j}$ is the noise residual, which must be perfectly zero in an ideal scenario.

If we now define $L_{ij} = n_{b_j} + n_{a_i} + 1$ and $L_{ji} = n_{a_j} + n_{b_i} + 1$, then it is trivial to show that $X_i\, G_{ij}$, for example, would be an $(L_{ij} + N - 2)$th-order polynomial in z^{-1}. Using the z-Transform definition, $X_i\, G_{ij}$ can be calculated as

$$X_i\, G_{ij} = \begin{bmatrix} x_i[0] & 0 & \cdots & 0 \\ \vdots & \cdots & \cdots & \vdots \\ x_i[L_{ij}-2] & x_i[L_{ij}-3] & \cdots & 0 \\ x_i[L_{ij}-1] & x_i[L_{ij}-2] & \cdots & x_i[0] \\ x_i[L_{ij}] & x_i[L_{ij}-1] & \cdots & x_i[1] \\ \vdots & \vdots & \ddots & \vdots \\ x_i[N-1] & x_i[N-2] & \cdots & x_i[N-L_{ij}] \\ 0 & x_i[N-1] & \cdots & x_i[N-L_{ij}+1] \\ \vdots & \cdots & \ddots & \vdots \\ 0 & \cdots & 0 & x_i[N-1] \end{bmatrix} \begin{bmatrix} G_{ij}[0] \\ G_{ij}[1] \\ \vdots \\ G_{ij}[L_{ij}-1] \end{bmatrix} \tag{10}$$

where $G_{ij}(z^{-1}) = G_{ij}[0] + G_{ij}[1]z^{-1} + \cdots + G_{ij}[L_{ij}-1]z^{-(L_{ij}-1)}$. A similar matrix representation can be written for $X_j\, G_{ji}$ as well. It is trivial to show that to satisfy Eq. (9), both $X_i\, G_{ij}$ and $X_j\, G_{ji}$ must have the same length. So, we can discard a few terms at the beginning and the end of signals $X_i\, G_{ij}$ and $X_j\, G_{ji}$, and rewrite Eq. (9) as

$$[\mathbf{X}_{ij} \quad -\mathbf{X}_{ji}] \begin{bmatrix} \boldsymbol{G}_{ij} \\ \boldsymbol{G}_{ji} \end{bmatrix} = \boldsymbol{E}_{i,j} \tag{11}$$

where

$$\mathbf{X}_{ij} = \begin{bmatrix} x_i[n_0^{i,j}] & x_i[n_0^{i,j}-1] & \cdots & x_i[n_0^{i,j}-L_{ij}+1] \\ \vdots & \vdots & \ddots & \vdots \\ x_i[n_0^{i,j}+W^{i,j}-1] & x_i[n_0^{i,j}+W^{i,j}-2] & \cdots & x_i[n_0^{i,j}+W^{i,j}-L_{ij}] \end{bmatrix}_{W^{i,j}\times L_{ij}} \tag{12}$$

$$\mathbf{X}_{ji} = \begin{bmatrix} x_j[n_0^{i,j}] & x_j[n_0^{i,j}-1] & \cdots & x_j[n_0^{i,j}-L_{ji}+1] \\ \vdots & \vdots & \ddots & \vdots \\ x_j[n_0^{i,j}+W^{i,j}-1] & x_j[n_0^{i,j}+W^{i,j}-2] & \cdots & x_j[n_0^{i,j}+W^{i,j}-L_{ji}] \end{bmatrix}_{W^{i,j}\times L_{ji}} \tag{13}$$

and $\boldsymbol{G}_{ij} = [G_{ij}[0] \quad G_{ij}[1] \quad \cdots \quad G_{ij}[L_{ij}-1]]^T$ and $\boldsymbol{G}_{ji} = [G_{ji}[0] \quad G_{ji}[1] \quad \cdots \quad G_{ji}[L_{ji}-1]]^T$. The term $\boldsymbol{E}_{i,j}$ is an $(L_{ij}+L_{ji}) \times 1$ vector containing noise errors. Start time ($n_0^{i,j}$) and time window ($W^{i,j}$) can be chosen any value greater than $\max(L_{ij}, L_{ji})$ and less than $W^{i,j} \leq N-1-n_0^{i,j}$, respectively.

Such CR expressions like Eq. (11) can be written between any pair of buildings. That is, we have a total of $n_p = P(P-1)/2$ CRs that can be stated as

$$\mathbf{X}\,\boldsymbol{G} = \boldsymbol{E} \tag{14}$$

where

$$\mathbf{X} = \begin{bmatrix} \mathbf{X}_{12} & -\mathbf{X}_{21} & & & & \\ & & \mathbf{X}_{13} & -\mathbf{X}_{31} & & \\ & & & & \ddots & \\ & & & & \mathbf{X}_{(P-1)P} & \mathbf{X}_{P(P-1)} \end{bmatrix} \tag{15}$$

$$\boldsymbol{G} = \left[\boldsymbol{G}_{12}{}^T, \boldsymbol{G}_{21}{}^T, \boldsymbol{G}_{13}{}^T, \boldsymbol{G}_{31}{}^T, \ldots, \boldsymbol{G}_{(P-1)P}{}^T, \boldsymbol{G}_{P(P-1)}{}^T\right]^T \tag{16}$$

$$\boldsymbol{E} = \left[\boldsymbol{E}_{1,2}{}^T \quad \boldsymbol{E}_{1,3}{}^T \quad \ldots \quad \boldsymbol{E}_{(P-1),P}{}^T\right]^T \tag{17}$$

In Eq. (14), matrix $\mathbf{X}$ is constructed by the building's response signals available through measurement, while vector $\boldsymbol{G}$ is composed of a_k and b_k coefficients of TFs of all buildings which are unknown and are going to be identified. Vector $\boldsymbol{E}$ is a noise vector. For simplicity, we select an equal time-window length W for all pairs, so matrix $\mathbf{X}$ is an $(n_p \times W) \times \left(\sum_{i=1}^{P}\sum_{j=i+1}^{P}(L_{ij}+L_{ji})\right)$ and set the start time index equal to $n_0 = \max(L_{ij})$ for $i,j = 1{:}P$ and $i \neq j$.

To solve the Eq. (14) we exactly use the Bayesian estimation introduced in Appendix A in which the Eq. (14) plays the role of the observation equation and $\boldsymbol{\theta}$ contains all unknown a_k and b_k coefficients of TFs of all buildings.

Deconvolution

Once the buildings are identified, it may look trivial to recover input excitations through deconvolution. That is,

$$S(z^{-1}) = \frac{X_i(z^{-1})}{H_i(z^{-1})} \tag{18}$$

and then

$$s[n] = \frac{1}{2\pi\sqrt{-1}} \oint S(z^{-1})\, z^{n-1} dz \tag{19}$$

where $n = t/\Delta t$ is discrete-time index and varies from 0 to $N-1$ with t and Δt denoting the time and sampling time interval, respectively. However, this inversion problem is only possible

if the system $1/H_i(z^{-1})$ is stable[2]. To satisfy this condition, the system $H_i(z^{-1})$ must not have any zeros outside of the unit circle, or in other words, it must be minimum phase [38], while it is most probably non-minimum phase.

A conventional way to calculate the inverse of a non-minimum phase system is through the Least-Squares Error (LSE). According to Eq. (1), we need to design an inverse FIR filter, $\boldsymbol{g}_{i_{n_{g_i}\times 1}}$, which satisfies

$$\boldsymbol{d} = \boldsymbol{h}_i * \boldsymbol{g}_i \tag{20}$$

where $\boldsymbol{d}_{\left(n_{h_i}+n_{g_i}-1\right)\times 1} = [1 \quad 0 \quad \cdots \quad 0]^T$. Convolving this filter with $x_i[n]$ results in recovering input motion. The Eq. (20) can be expressed in a matrix form as

$$\mathbf{H}_i\, \boldsymbol{g}_i = \boldsymbol{d} \tag{21}$$

with

$$\mathbf{H}_{i_{\left(n_{h_i}+n_{g_i}-1\right)\times n_{g_i}}} = \begin{bmatrix} h_i[0] & & & \\ h_i[1] & h_i[0] & & \\ & h_i[1] & \ddots & \\ h_i\left[n_{h_i}-1\right] & & & h_i[0] \\ & h_i\left[n_{h_i}-1\right] & & h_i[1] \\ & & \ddots & \\ & & & h_i\left[n_{h_i}-1\right] \end{bmatrix}, \tag{22}$$

As the number of the columns of the matrix $\mathbf{H}_i$ is less than that of the rows, the coefficients of the FIR filter are computed in an approximate LSE way as $\boldsymbol{g}_i = \mathbf{H}_i{}^{\dagger}\boldsymbol{d}$ where † is the Moore-Penrose pseudo-inverse operator. Therefore, it is impossible to realize the exact inverse of a linear FIR system using this method. Moreover, because $\boldsymbol{g}_i$ is non-minimum phase the error energy $(\boldsymbol{d} - \mathbf{H}_i\, \boldsymbol{g}_i)^T(\boldsymbol{d} - \mathbf{H}_i\, \boldsymbol{g}_i)$ does not converge to zero [39].

Fortunately, as the input excitation is measured by at least another building, there is a possibility to exactly recover it. For example, if we can identify inverse filters $\boldsymbol{g}_i$ and $\boldsymbol{g}_j$ satisfying the following equation

$$\boldsymbol{d} = \boldsymbol{h}_i * \boldsymbol{g}_i + \boldsymbol{h}_j * \boldsymbol{g}_j \tag{23}$$

we can recover common input excitation through

$$\boldsymbol{s} = \boldsymbol{x}_i * \boldsymbol{g}_i + \boldsymbol{x}_j * \boldsymbol{g}_j \tag{24}$$

To identify these inverse filters, let's set $n_{g_i} = n_{h_j} - 1$ and $n_{g_j} = n_{h_i} - 1$. Then, we have

[2] Bounded-Input Bounded-Output (BIBO) condition.

$$[\mathbf{H}_i \quad \mathbf{H}_j] \begin{bmatrix} \boldsymbol{g}_i \\ \boldsymbol{g}_j \end{bmatrix} = \boldsymbol{d} \tag{25}$$

in which matrix $[\mathbf{H}_i \quad \mathbf{H}_j]$ is square and the exact solution can be recovered through matrix inversion [39]. However, the solution is only available if these two buildings do not share common zeros, which is not the case in our problem as discussed before. Herein, we propose a modification to the deconvolution to reduce the chance of having common zeros [40].

Time convolution of the Eq. (1) can be expressed in the time-frequency domain using Short-Time-Fourier-Transform (STFT) as follows [41]

$$\underline{x}_i[p,k] = \sum_{k'=0}^{N_w-1} \sum_{p'=0}^{Q_i-1} \underline{s}[p-p',k']\,\underline{h}_i[p',k,k'] \tag{26}$$

where underbar represents STFT representation, N_w is the number of frequencies, and Q_i is the length of IRF in STFT domain. The IRF in the STFT domain ($\underline{h}_i[p',k,k']$) is called a cross-band filter. Neglecting effects of the neighbor frequencies, we can approximate response at each frequency using its band-to-band version ($\tilde{\underline{h}}_i[p',k]$) which is Convolutive Transfer Function (CTF) as

$$\underline{x}_i[p,k] \approx \sum_{p'=0}^{Q_i-1} \underline{s}[p-p',k]\,\tilde{\underline{h}}_i[p',k] \tag{27}$$

which is a convolution at each frequency index of k as

$$\underline{\boldsymbol{x}}_i \approx \tilde{\underline{\boldsymbol{h}}}_i * \underline{\boldsymbol{s}} \tag{28}$$

which is similar to the time convolution. So, we can follow the same approach described above to recover $\underline{\boldsymbol{s}}$ at each frequency and then transform the solution to the time domain through inverse STFT. That is, we are looking for $\underline{\boldsymbol{g}}_i$s filters which satisfy the following relationship

$$\boldsymbol{d} = \sum_{1}^{n_B} \tilde{\underline{\boldsymbol{h}}}_i * \underline{\boldsymbol{g}}_i \tag{29}$$

where n_B is the number of buildings. Now a similar solution introduced in Eq. (25) can be used to estimate inverse CTFs and consequently recover input excitation. Contrary to the time domain solution, the CTFs have very short length and the chance of having common zero among the buildings significantly reduces.

Verification

To verify the method, the response of four shear buildings with a various number of stories from 3 to 7 are generated under Elcentro ground acceleration. **Figure 10** shows the recorded time histories and the exact Transfer Functions (green curves). We carried out the proposed TF-based CR method by starting at those red initial TFs. The final results are shown in blue and black. The blue curves show the TFs constructed by mean values of the coefficients,

while the black curves are the means of the TFs. As seen, the estimated TFs (black and blues curves) are perfectly matched to the exact TFs except very high-frequency region. Note that the response signals are polluted with random noises with Root-Mean-Squares (RMS) equal to 5% of the RMS of the noise-free signals. As the solution is obtained through a stochastic filtering approach, the variance of the estimated results is also shown in **Figure 10** through mean ± 1 standard deviation. As seen, the estimated results are highly reliable. We then employed the proposed STFT deconvolution solution to recover common input motion. A comparison between the recovered one and the exact one is shown in **Figure 11**. As seen, the input motion is almost identical to the exact time history.

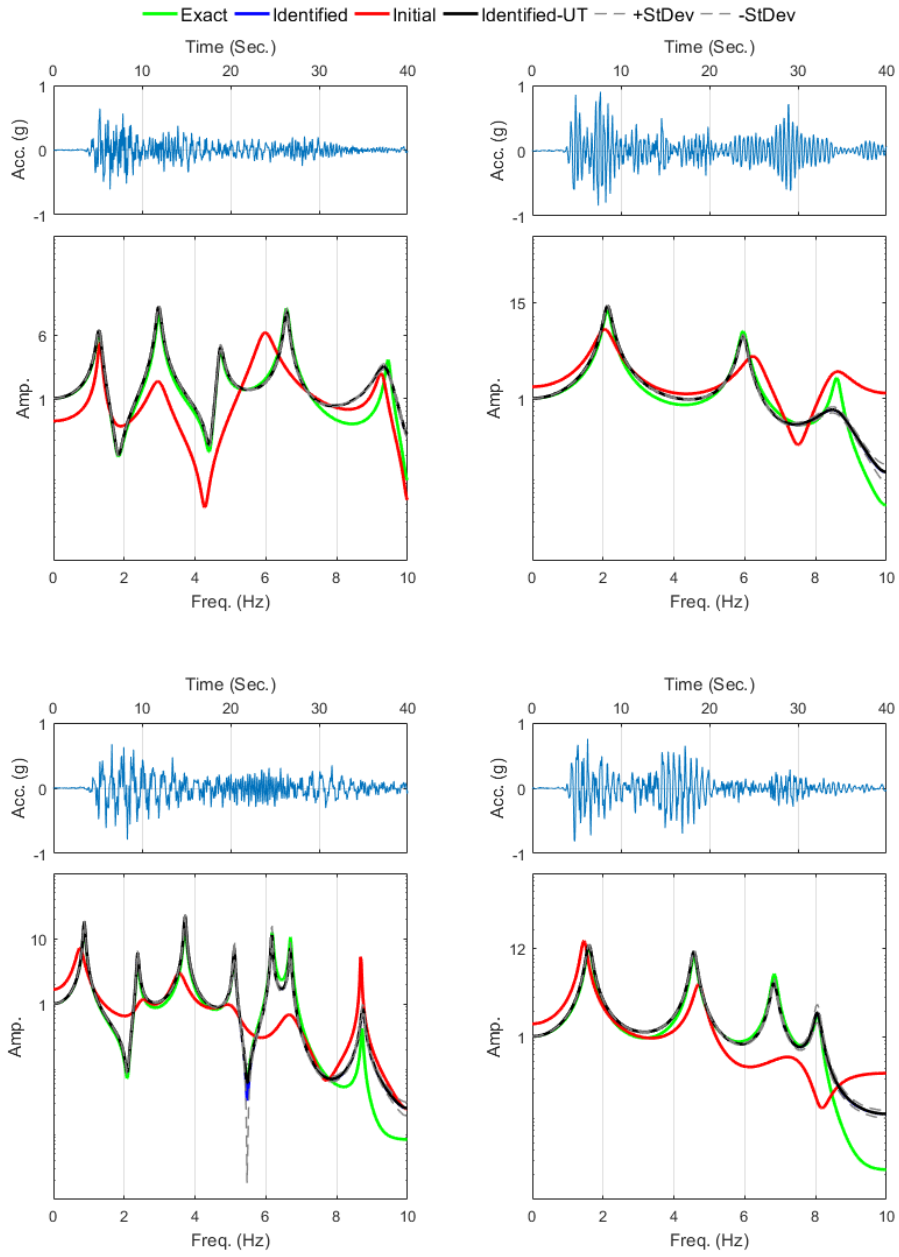

Figure 10. Results of the verification study.

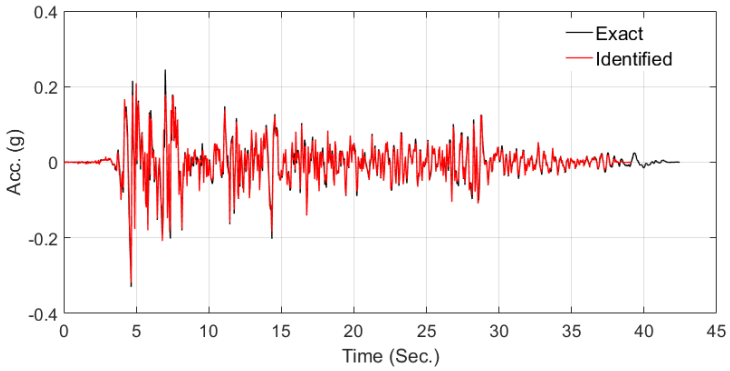

Figure 11. Comparison between exact and recovered input motion.

Validation

To validate the method, data recorded on two neighboring buildings in downtown San Francisco (CSMIP stations #58411 and #58412 are used (see **Figure 12**). Data recorded in the East-West direction during the recent 2014 South Napa earthquake is studied here. **Figure 13** displays a comparison between the recorded signals at the foundation levels of these two buildings, both of which are assumed here to be input motions. As seen, these two signals are quite similar and have a correlation coefficient [42] >76%, and as such, they satisfy the major assumption of the proposed method.

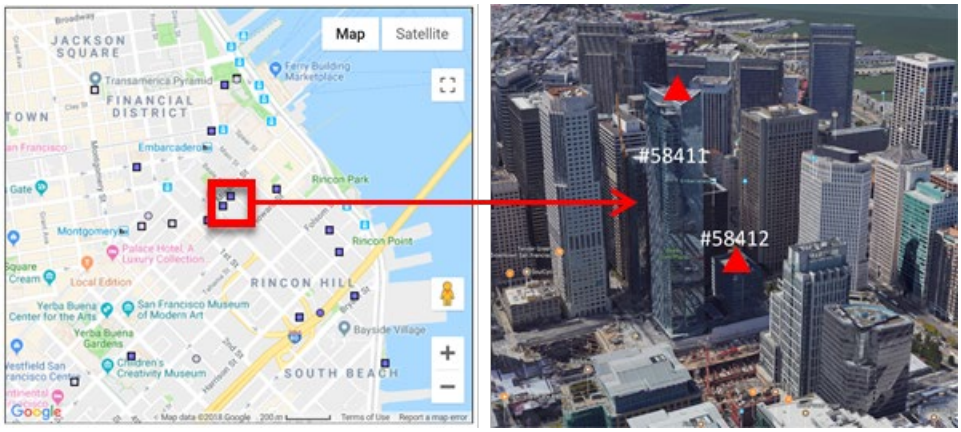

Figure 12. Chosen buildings for the validation study.

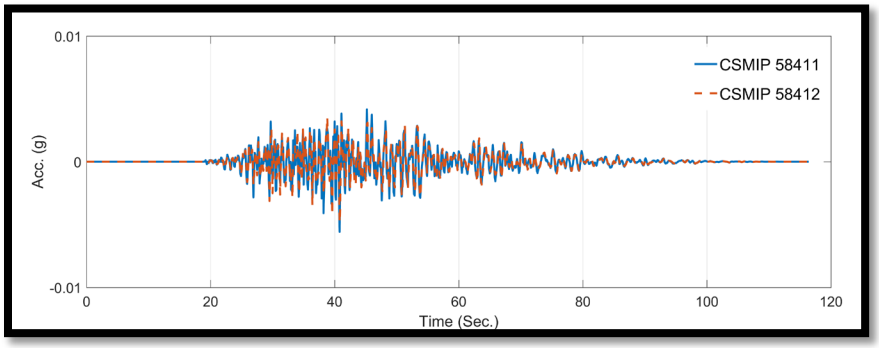

Figure 13. 76% similarity between recorded signals at the foundations of two buildings.

To carry out the identification process, we use signals recorded at the roof level—i.e., channel #29 for CSMIP58411, and the average of channels #11 and #12 for CSMIP58412, which are located at the two opposing ends of roof floor. We only use 50 seconds of the intense portion of the signals, because the level of vibration is too low during other times. **Figure 14** shows again the exact TFs in green which are empirically calculated using input and output signals, the initial TFs in red, and the identified TFs in black and blue. As seen, the final results are quite matched to the exact ones with a negligible variation.

Finally, we extracted common input excitation which is compared to the measured foundation responses (assumed here as exact input motions) in **Figure 15**. It is quite interesting to note that there is almost a 76% similarity between the recovered input motion and each of these foundation responses, showing the method works very well.

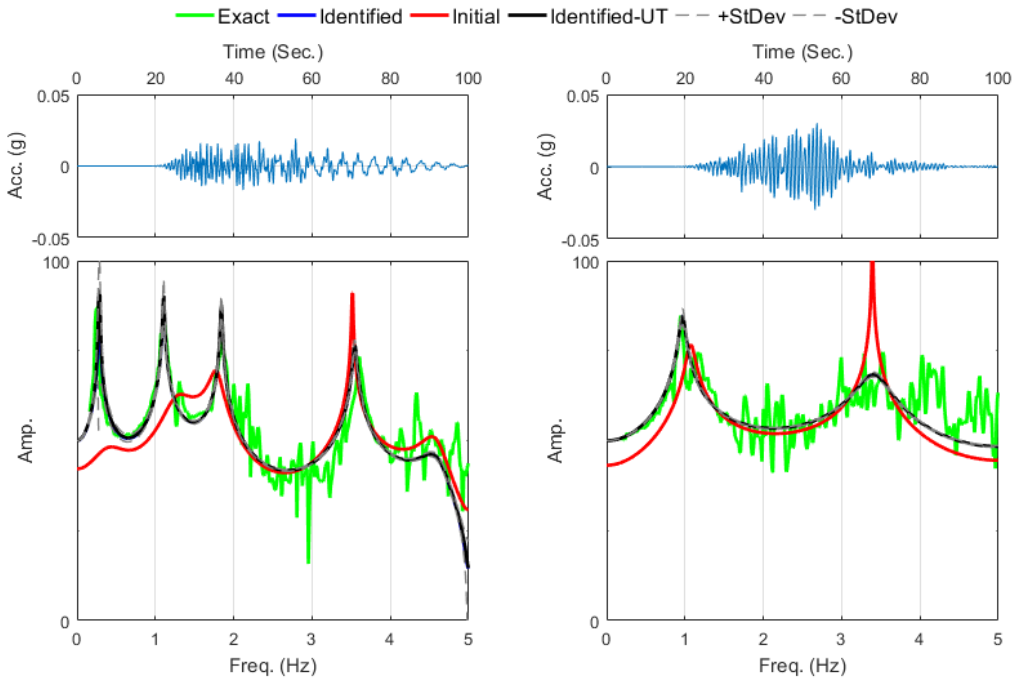

Figure 14. Results of the validation study.

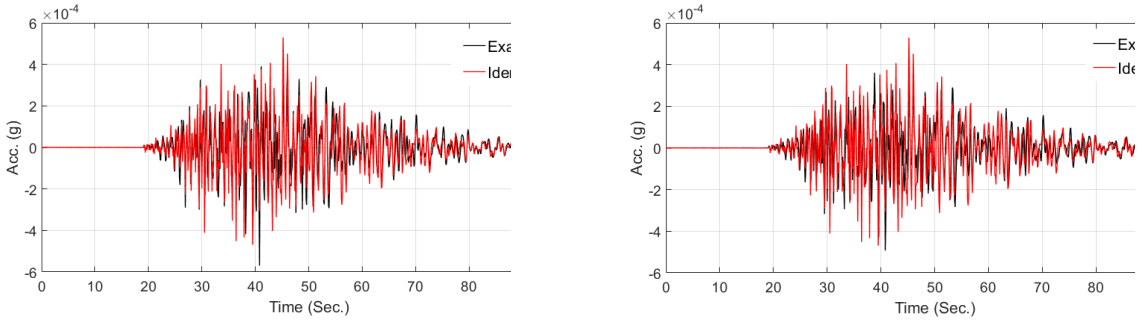

Figure 15. Comparison between recovered input motion and recorded foundation responses.

Modal-Based CR Method

The initial guess in the proposed CR method is sometimes important because the problem is not convex and could have various local solutions. To make the method more robust we replaced the Transfer Function formula with an IRF constructed using superposition of analytical modal IRFs as shown in the following equation

$$h[k\Delta t] = \Delta t \sum_{m=1}^{n_m} \frac{\beta_m \varphi_{r,m}}{\omega_{d_m}} e^{-\xi_m \omega_{n_m} k\Delta t} \left[\left({\omega_{d_m}}^2 - {\xi_m}^2 {\omega_{n_m}}^2 \right) \sin(\omega_{d_m} k\Delta t) + 2\xi_m \omega_{n_m} \cos(\omega_{d_m} k\Delta t) \right] \tag{30}$$

where ω_{n_m}, ξ_m, β_m, and $\varphi_{r,m}$ are m-th mode natural frequency, damping ratio, contribution factor, and modal deformation, respectively, and $\omega_{d_m} = \omega_{n_m}\sqrt{1 - {\xi_m}^2}$. By using this closed-form solution, we now have parameters with physical meaning. So, we can set initial point more accurately. More importantly, we can put constraints on the parameters. For example, we know that natural frequencies and damping ratios are positive. Or natural frequencies must be increasing values. Also, we can limit the frequency of interest according to the frequency content of the recorded responses.

Verification

To verify the modal-based version of the CR method, we simulated the response of a 5-story and a 3-story shear buildings whose modal properties are reported in **Table 4**. The responses ate the roof were polluted with random noises to have signals with Signal-to-Noise Ratio (SNR) of 40. Before carrying out the identification, signals were filtered by a low-pass filter with cut-off frequency of 15 Hz, as there is no energy above this frequency in the 3-story response.

Table 4. Analytical modal properties.

	5-Story Building					3-Story Building		
Modes	1	2	3	4	5	1	2	3
$f_n(Hz)$	2.22	5.12	8.09	11.33	16.27	3.17	8.88	12.83
$\xi_n(\%)$	5.00	4.18	5.00	6.26	8.42	5.00	4.21	5.00
$\varphi_{rn}\beta_n$	1.41	-0.54	0.15	-0.02	0.0006	1.22	-0.28	0.06

To see the accuracy of the identified modal properties or actually systems, simulated responses are compared with the responses predicted by using exact input motion and identified modal properties in **Figure 16**. As seen, both buildings are identified perfectly. The recovered input motion is compared with the exact one in **Figure 17** in the frequency domain. As observed, the recovered input motion is highly accurate.

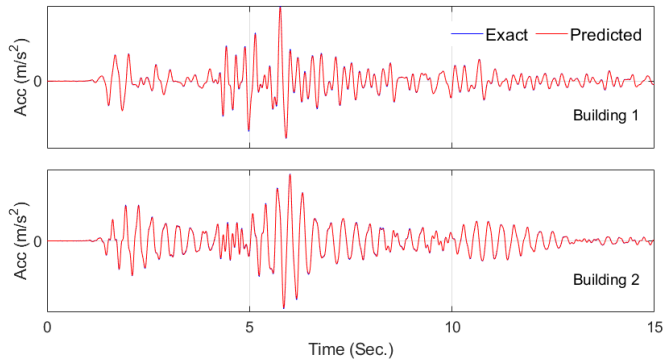

Figure 16. Comparison between simulated responses with predicted responses using identified modal properties and exact input motion.

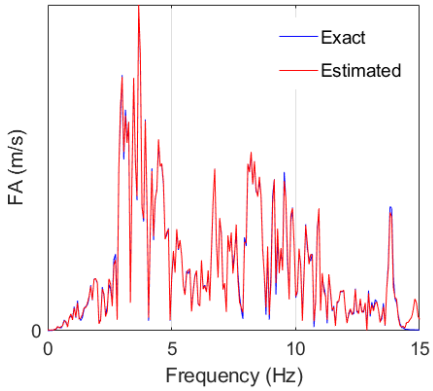

Figure 17. Comparison between exact and recovered input motion in the frequency domain.

Validation

To validate the method, we used a new set of buildings not to be limited to a specific case. **Figure 18** shows these two buildings with less than 500 meters distance. They are oriented in the same direction, so we can use our 2D modal-based CR approach. There are two nearby free-field stations, but one of them is no longer working. We use data recorded in the NS directions of these buildings at the roof level during July 5th 2019 Ridgecrest earthquake. In the first step, we need to specify the frequency range of interest and the probable number of modes. **Figure 19** shows the Fourier spectra of the two signals. As seen, we may be able to recover input motion up to 6 Hz. In this frequency range, the CSMIP24517 building seems to have 2 modes while the other building could have up to 3 modes. Using two response signals, we carried out the estimation and **Figure 20** shows a comparison between the recovered FIM in time and frequency domains with the recorded FFM. As seen, these two signals are very similar, which validates the performance of the proposed method.

Figure 18. Buildings used for validation of the modal-based CR method.

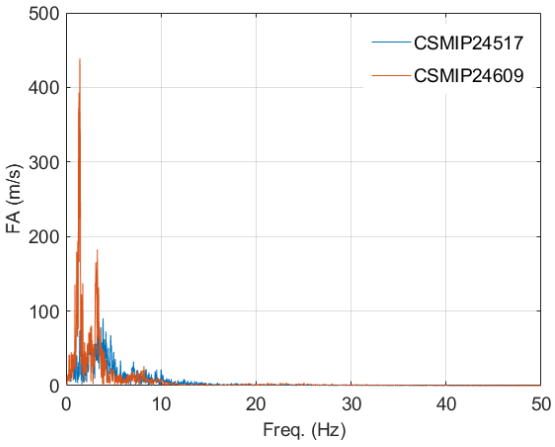

Figure 19. Fourier spectra of the response of two buildings.

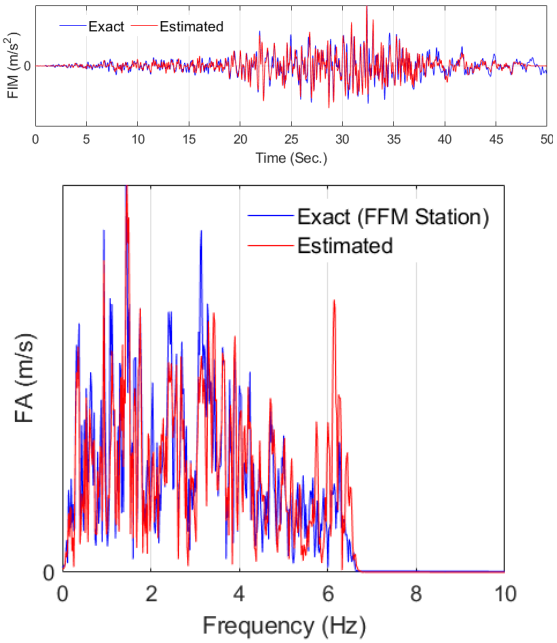

Figure 20. Comparison between identified input motion and recorded FFM in (top) time and (bottom) frequency domain.

Application

As another example, **Figure 21** shows two buildings with almost 500 meters distance. We use their roof response in NS direction recorded in Alumrock 2007 earthquake. Based on the Fourier spectra (not shown here), we consider frequencies below 10 Hz to make sure both signals have enough energy. Five and four modes are considered for CSMIP57355 and CSMIP57356 buildings, respectively.

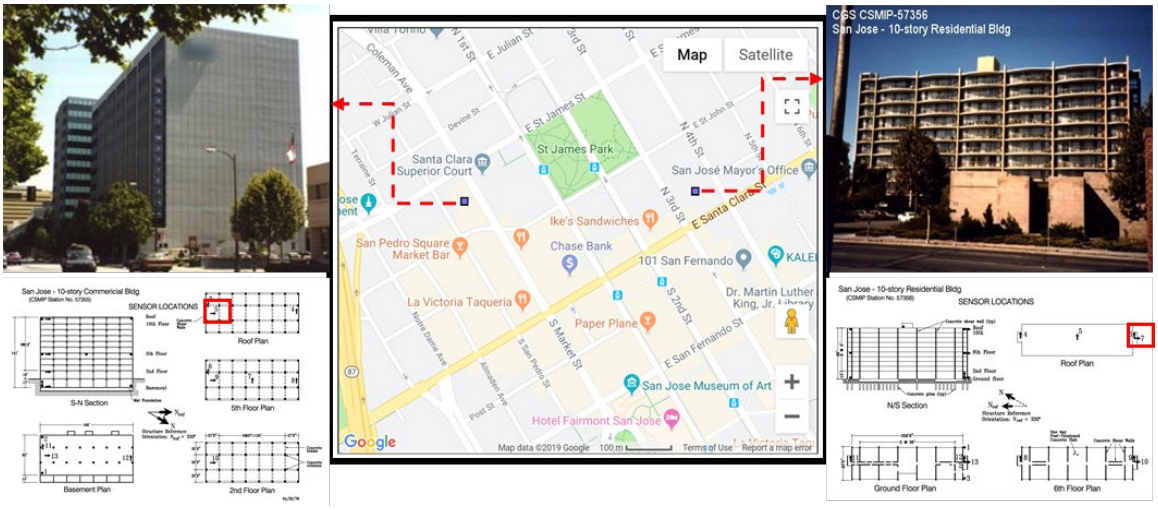

Figure 21. Buildings used for application study of the modal-based CR method.

As no FFM is recorded, a comparison between identified input motion and recorded foundation responses is shown in **Figure 22** in time and frequency domains. The correlation analysis shows that there is almost 80% similarity between foundation responses and this identified input motion.

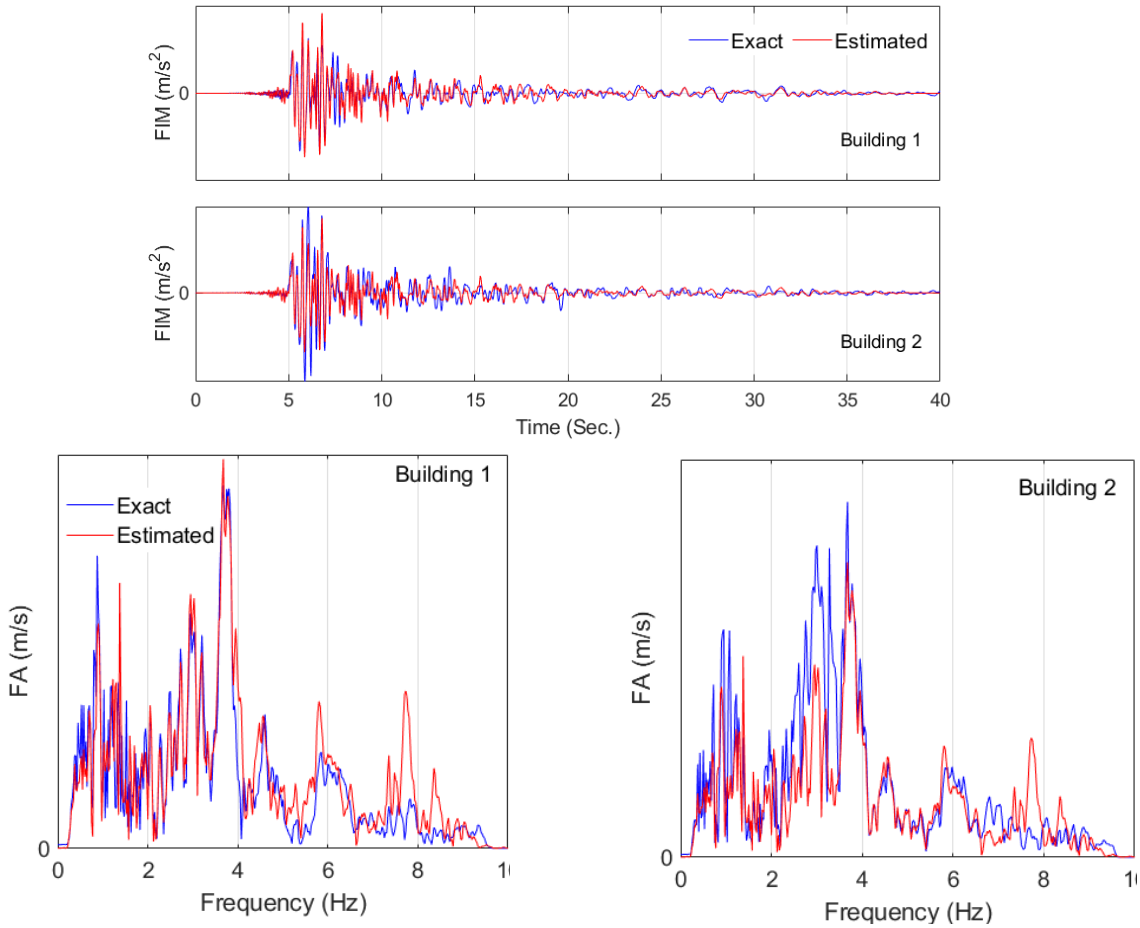

Figure 22. Comparison between recorded foundation responses (blue) and the identified input motion. Building 1 is CSMIP57355 and Building 2 is CSMIP57356.

Model-Based CR Method

In real-life, there is no guarantee to have adjacent buildings aligned in the same direction. So, the CR method should be extended to a more general 3D problem. While it is theoretically possible to use the TF-based or modal-based CR solutions to the 3D cases, the number of parameters to be estimated will be huge. In this section, a hybrid solution is proposed in which model-based Bayesian estimation is combined with the original CR solution to take advantage of benefits of each one [43].

Assume that two buildings are excited under similar bidirectional ground accelerations $\ddot{\boldsymbol{x}}_g$ and $\ddot{\boldsymbol{y}}_g$. Assume that the buildings remain linear-elastic, do not exhibit lateral-torsional

coupling, and are instrumented in their local principal directions x and y as shown in **Figure 23**. The recorded absolute acceleration responses of Building 1 can be written as a linear discrete convolution of the input motions and the building's IRF as

$$\ddot{\boldsymbol{x}}_1 = \boldsymbol{h}_1^x * \left[\ddot{\boldsymbol{x}}_g \cos\alpha + \ddot{\boldsymbol{y}}_g \sin\alpha\right] + \boldsymbol{v}_1, \tag{31}$$

$$\ddot{\boldsymbol{y}}_1 = \boldsymbol{h}_1^y * \left[-\ddot{\boldsymbol{x}}_g \sin\alpha + \ddot{\boldsymbol{y}}_g \cos\alpha\right] + \boldsymbol{w}_1, \tag{32}$$

where $\boldsymbol{h}_1^x$ and $\boldsymbol{h}_1^y$ are the building's IRFs in local x and y directions, respectively; and $\boldsymbol{v}_1$ and $\boldsymbol{w}_1$ represent the corresponding measurement noises, which are assumed to be zero-mean, spatially uncorrelated Gaussian white signals.

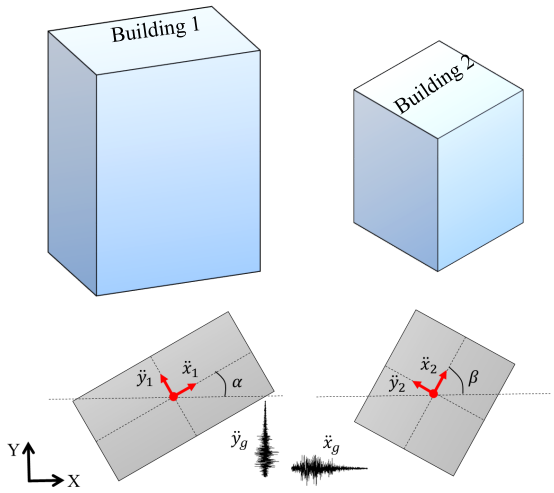

Figure 23. Two adjacent instrumented buildings under a bidirectional seismic excitation.

It is straightforward to combine Eqs. (1) and (2) to come up with equations that contain only a unidirectional earthquake excitation as follows

$$\ddot{\boldsymbol{x}}_1 * \boldsymbol{h}_1^y \sin\alpha + \ddot{\boldsymbol{y}}_1 * \boldsymbol{h}_1^x \cos\alpha = \boldsymbol{h}_1 * \ddot{\boldsymbol{y}}_g + \bar{\boldsymbol{v}}_1 + \bar{\boldsymbol{w}}_1 \tag{33}$$

$$\ddot{\boldsymbol{x}}_1 * \boldsymbol{h}_1^y \cos\alpha - \ddot{\boldsymbol{y}}_1 * \boldsymbol{h}_1^x \sin\alpha = \boldsymbol{h}_1 * \ddot{\boldsymbol{x}}_g + \tilde{\boldsymbol{v}}_1 + \tilde{\boldsymbol{w}}_1, \tag{34}$$

where

$$\boldsymbol{h}_1 = \boldsymbol{h}_1^x * \boldsymbol{h}_1^y, \tag{35}$$

and $\bar{\boldsymbol{v}}_1 = \boldsymbol{v}_1 * \boldsymbol{h}_1^y \sin\alpha$, $\bar{\boldsymbol{w}}_1 = \boldsymbol{w}_1 * \boldsymbol{h}_1^x \cos\alpha$, $\tilde{\boldsymbol{v}}_1 = \boldsymbol{v}_1 * \boldsymbol{h}_1^y \cos\alpha$ and $\tilde{\boldsymbol{w}}_1 = -\boldsymbol{w}_1 * \boldsymbol{h}_1^x \sin\alpha$ are colored noises. Similar equations can be written for the other building by replacing the subscript "1" with "2" and the orientation angle α with β as

$$\ddot{\boldsymbol{x}}_2 * \boldsymbol{h}_2^y \sin\beta + \ddot{\boldsymbol{y}}_2 * \boldsymbol{h}_2^x \cos\beta = \boldsymbol{h}_2 * \ddot{\boldsymbol{y}}_g + \bar{\boldsymbol{v}}_2 + \bar{\boldsymbol{w}}_2 \tag{36}$$

$$\ddot{x}_2 * h_2^y \cos\beta - \ddot{y}_2 * h_2^x \sin\beta = h_2 * \ddot{x}_g + \tilde{v}_2 + \tilde{w}_2, \tag{37}$$

where $h_2 = h_2^x * h_2^y$, $\bar{v}_2 = v_2 * h_2^y \sin\beta$, $\bar{w}_2 = w_2 * h_2^x \cos\beta$, $\tilde{v}_2 = v_2 * h_2^y \cos\beta$, and $\tilde{w}_2 = -w_2 * h_2^x \sin\beta$. Following the CR method, we convolve both sides of Eqs. (33)/(34) and (36)/(37), respectively, by h_2 and h_1, to get

$$\{\ddot{x}_1 * h_1^y \sin\alpha + \ddot{y}_1 * h_1^x \cos\alpha\} * h_2 - \{\ddot{x}_2 * h_2^y \sin\beta + \ddot{y}_2 * h_2^x \cos\beta\} * h_1 = \bar{r} \tag{38}$$

$$\{\ddot{x}_1 * h_1^y \cos\alpha - \ddot{y}_1 * h_1^x \sin\alpha\} * h_2 - \{\ddot{x}_2 * h_2^y \cos\beta - \ddot{y}_2 * h_2^x \sin\beta\} * h_1 = \tilde{r}, \tag{39}$$

where

$$\bar{r} = h_2 * (\bar{v}_1 + \bar{w}_1) - h_1 * (\bar{v}_2 + \bar{w}_2) \tag{40}$$

$$\tilde{r} = h_2 * (\tilde{v}_1 + \tilde{w}_1) - h_1 * (\tilde{v}_2 + \tilde{w}_2). \tag{41}$$

In Eqs. (40) and (41), $\bar{r}$ and $\tilde{r}$ are the remainders that represent the difference between the ideal case of noiseless measurements and the realistic case of noisy measurements. We assume that initial numerical models of the two buildings are available, and our objective is to identify/update their corresponding model parameters. Based on this assumption, Eqs. (3) and (39) can be rewritten as

$$\{y_1\langle\ddot{x}_1 \sin\alpha\rangle + x_1\langle\ddot{y}_1 \cos\alpha\rangle\} * h_2 - \{y_2\langle\ddot{x}_2 \sin\beta\rangle + x_2\langle\ddot{y}_2 \cos\beta\rangle\} * h_1 = \bar{r} \tag{42}$$

$$\{y_1\langle\ddot{x}_1 \cos\alpha\rangle + x_1\langle-\ddot{y}_1 \sin\alpha\rangle\} * h_2 - \{y_2\langle\ddot{x}_2 \cos\beta\rangle + x_2\langle\ddot{y}_2 \sin\beta\rangle\} * h_1 = \tilde{r}, \tag{43}$$

where, for example, $y_1\langle\ddot{x}_1 \sin\alpha\rangle$ stands for the response of Building 1 in its y direction under the input excitation $\ddot{x}_1 \sin\alpha$. The components of Eqs. (42) and (13) can be derived easily. For example, the first part of Eq. (42)—i.e., $\{y_1\langle\ddot{x}_1 \sin\alpha\rangle + x_1\langle\ddot{y}_1 \cos\alpha\rangle\} * h_2$—can be calculated as follows: First, $y_1\langle\ddot{x}_1 \sin\alpha\rangle$ and $x_1\langle\ddot{y}_1 \cos\alpha\rangle$ are estimated. Then, they are used as input excitation in the x-direction of Building 2. The resulting response time history is then used as input excitation for Building 2 in the y-direction, since $h_2 = h_2^x * h_2^y$. The resulting response time history of Building 2 in the y-direction represents the first part of the Eq. (42).

Eqs. (42) and (13) are used as the observation equation within the Bayesian estimation framework where FE models are used to carry out all the predictions and the vector θ parameters of the structural models. Through this hybrid solution, we avoid adding unknown input motions to the updating parameters which substantially reduces computational cost. Also, the Fe models provide the opportunity to reduce number of structural parameters to be estimated.

Deconvolution

Since the two buildings have been fully identified, the common ground motions, $\ddot{x}_g$ and $\ddot{y}_g$, can be recovered from the buildings' responses via deconvolution. Herein, we suggest another deconvolution approach because we have two input motions. Let us assume a noise-free version of the discrete-time convolution in Eq. (31) in the matrix form as

$$\mathbf{A}_{N\times N}\,\boldsymbol{x}_{N\times 1} = \boldsymbol{b}_{N\times 1} \tag{44}$$

with

$$\boldsymbol{b} = [\ddot{x}_1[0] \quad \cdots \quad \ddot{x}_1[N-1]]^T \tag{45}$$

$$\boldsymbol{x} = [\ddot{x}_g[0]\cos\alpha + \ddot{y}_g[0]\sin\alpha \quad \cdots \quad \ddot{x}_g[N-1]\cos\alpha + \ddot{y}_g[N-1]\sin\alpha]^T \tag{46}$$

$$\mathbf{A} = \begin{bmatrix} h_1^x[0] & & & & & & \\ h_1^x[1] & h_1^x[0] & & & & & \\ \vdots & & \ddots & & & & \\ h_1^x[L_1^x-1] & h_1^x[L_1^x-2] & \cdots & h_1^x[0] & & & \\ 0 & h_1^x[L_1^x-1] & \ddots & \cdots & h_1^x[0] & & \\ \vdots & & & & & \ddots & \\ 0 & \cdots & 0 & h_1^x[L_1^x-1] & h_1^x[L_1^x-2] & & h_1^x[0] \end{bmatrix}, \tag{47}$$

wherein L_1^x is the effective length of the first building's IRF in its local x-direction. The matrix $\mathbf{A}$ can be ill-conditioned, which means that the vector $\boldsymbol{x}$ cannot be recovered by a matrix inversion [44]. To resolve the ill-conditioning problem of matrix $\mathbf{A}$, we have to replace this matrix with its closest well-conditioned approximation.

Matrix $\mathbf{A}$ has a Toeplitz structure; that is, it has equal elements across the main diagonal and the sub-diagonals parallel to the main diagonal (our systems are causal, so their matrices are lower triangular). It has been shown [45] that for each Toeplitz matrix, a well-conditioned circulant matrix can be found that is asymptotically equivalent to the Toeplitz matrix. To recover the ground motions from each building's response, we invert the asymptotically equivalent circulant matrix corresponding to $\mathbf{A}$. By constructing another similar matrix representation—as Eq. (44) corresponds to Eq. (2)—, we can backcalculate the ground motion vectors $\ddot{\boldsymbol{x}}_g$ and $\ddot{\boldsymbol{y}}_g$ in the global coordinate system as follows

$$\begin{bmatrix} \ddot{\boldsymbol{x}}_g \\ \ddot{\boldsymbol{y}}_g \end{bmatrix} = \begin{bmatrix} \cos\alpha & \sin\alpha \\ -\sin\alpha & \cos\alpha \end{bmatrix}^{-1} \begin{bmatrix} \left(\mathbf{C}_{1,x}^{-1}\,\ddot{\boldsymbol{x}}_1\right)^T \\ \left(\mathbf{C}_{1,y}^{-1}\,\ddot{\boldsymbol{y}}_1\right)^T \end{bmatrix} \tag{48}$$

where $\mathbf{C}_{1,x}$ and $\mathbf{C}_{1,y}$ are the circulant matrices constructed using matrix $\mathbf{A}$ for the local x and y directions [45], respectively. Indeed, the ground motions can also be recovered from responses of the second building, which must be identical in ideal conditions (noise-free and perfect identification results).

Verification

To verify the proposed identification method, we created two three-dimensional building models using SAP2000 [32] as shown in **Figure 24**. The details of these models can be found in [43]. To simulate the seismic responses of the two buildings, we applied the East-West (EW) and the North-South (NS) ground motions recorded at the El Centro station during the 1940 Imperial Valley earthquake in the global X and Y directions, respectively. The roof absolute acceleration response time histories in local x and y directions of the two buildings are used for the

identification. Independent random noises with $0.005\ m^2/sec^4$ variance (corresponding to signals with 0.7%g root mean square amplitude) is added to the simulated time histories to mimic in noisy measurements.

The proposed system identification is utilized to estimate the unknown parameters, which consist of parameters characterizing the soil-foundation impedance functions and superstructure's parameters as

$$\boldsymbol{\theta} = \left[K_x^1, K_y^1, K_{xx}^1, K_{yy}^1, C_x^1, C_y^1, W_w^1, \alpha_1, \beta_1, K_x^2, K_y^2, K_{xx}^2, K_{yy}^2, C_x^2, C_y^2, W_w^2, \alpha_2, \beta_2\right]^T \tag{49}$$

where K and C represent soil spring stiffness and soil dashpot viscosity, and superscripts and subscripts denote the building number and the direction, respectively. W_w^1 and W_w^2 are the equivalent widths of the infill walls in Buildings 1 and 2, respectively. Also, parameters α_1, β_1, and α_2, β_2 are mass- and stiffness-proportional Rayleigh damping coefficients of Buildings 1 and 2, respectively. The "true" values of these parameters are provided in **Table 5**.

Table 5. Exact values of the updating parameter candidates.

Building No.	1	2	3	4	5	6	7	8	9
1	K_x (GN/m)	K_y (GN/m)	K_{xx} (GNm)	K_{yy} (GNm)	C_x (MNs/m)	C_y (MNs/m)	W_w (m)	α (1/s)	β (1000s)
	3.33	3.44	156	283	89	89	0.5	0.90	0.27
Building No.	10	11	12	13	14	15	16	17	18
2	K_x (GN/m)	K_y (GN/m)	K_{xx} (GNm)	K_{yy} (GNm)	C_x (MNs/m)	C_y (MNs/m)	W_w (m)	α (1/s)	β (1000s)
	1.93	2.05	25	69	30	30	0.5	0.83	0.26

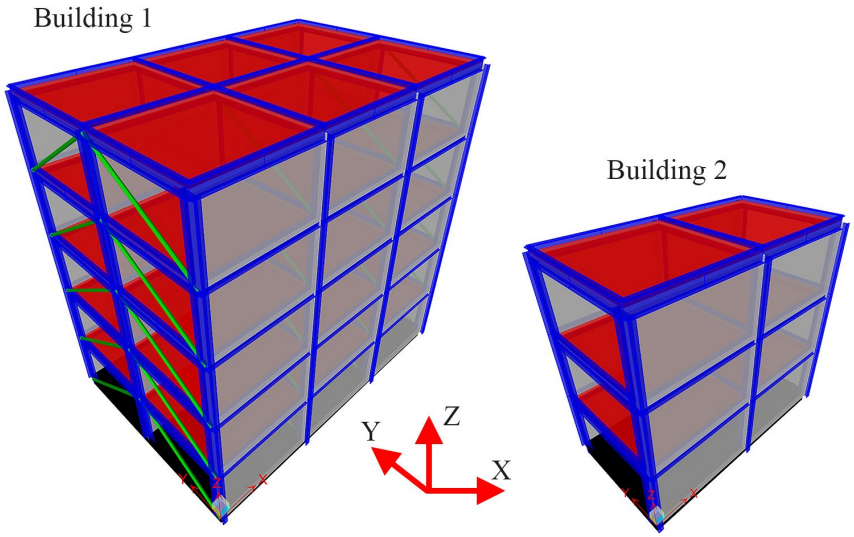

Figure 24. Two adjacent buildings used for verification study.

After carrying out an extensive identifiability study, which is another specific benefit of the proposed method and can be found in the original reference [43], the list of updating parameters was reduced to $\boldsymbol{\theta} = [K_x^1, K_{xx}^1, W_w^1, \alpha_1, K_x^2, K_{xx}^2, W_w^2, \alpha_2]^T$ and other parameters fixed at

their true values. **Table 6** shows the results of the identification along with the estimation Coefficient of Variation (COV). As seen, all unknown parameters, except K_x^2 , are identified with small final errors and near-zero COVs. K_x^2 is the parameter that we added to our updating parameters list despite the fact that it had a relatively strong dependence on W_w^2. As seen in **Table 6**, this dependency results in an inaccurate estimation of W_w^2 as well. The estimated COVs can be used to assess the estimation uncertainties, the higher the COV, the less reliable the estimation is. **Table 6** shows that the COV of K_x^2 is approximately 3 times larger than other parameters, which means that the identified parameter value for K_x^2 is relatively less reliable than other parameters.

Table 6. Identified mean errors and COVs through.

ID No.	1	3	7	8	10	12	16	17
Parameters	K_x^1	K_{xx}^1	W_w^1	α_1	K_x^2	K_{xx}^2	W_w^2	α_2
Final Error (%)	0.96	–0.57	–0.15	3.08	23.29	–2.07	–5.25	1.49
Final COV (%)	0.96	0.55	0.51	1.04	3.90	0.57	0.99	0.92

To evaluate the accuracy of the identification results and the effects of estimation errors, the response of buildings are generated using the identified parameters and using exact ground motions. The responses are compared with the noise-free measured (simulated using exact parameter values) responses in **Figure 25**. As can be seen, the predicted responses match the exact responses. This means that the combined effects of 23% error in K_x^2 and 5% error in W_w^2 do not significantly affect the response of Building 2 in its x-direction.

Finally, having identified the FE models of the buildings, we recover the input ground motions in global directions using the deconvolution approach. The input motions backcalculated using each building's recoded responses are shown in **Figure 26**. As seen, the recovered ground motions from both buildings' responses match the exact input motions.

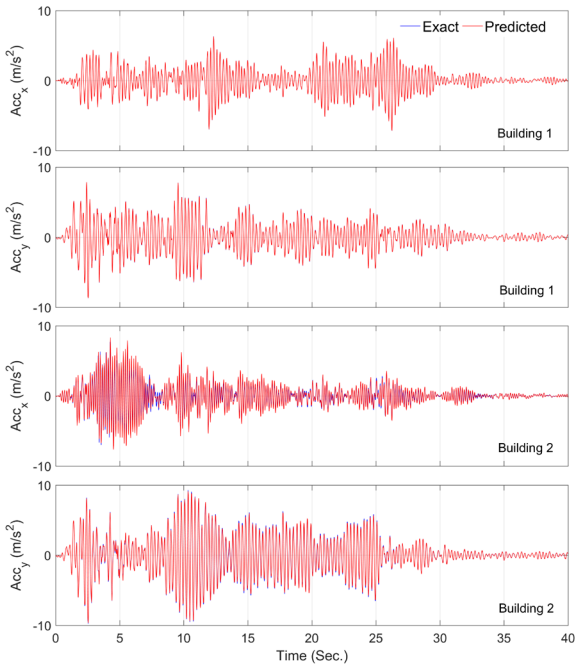

Figure 25. Comparison of the predicted and exact building responses.

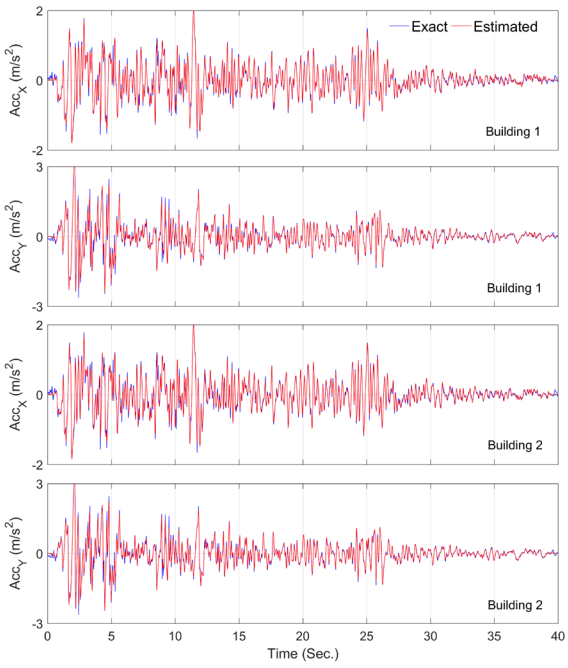

Figure 26. Comparison of the recovered and exact input motions.

Conclusions

Earthquake input excitation to the building structures may be unavailable in various conditions. Soil-Structure Interaction (SSI) effects may prevent measuring true input excitation through both inertial and kinematic effects. Also, input excitation may be lost due to sensor malfunctioning or recorded with low resolution. The present study proposed various methods to be able to extract input excitation from responses recorded by instrumented buildings like CSMIP buildings. The proposed methods range from sophisticated and computationally demanding model-based output-only Bayesian estimation to simple but practical data-driven Cross-Relation (CR) method in which needed additional information is taken from response of the adjacent buildings. We successfully verified and validated all these methods using simulated and real-life data, respectively. A hybrid method was also proposed by a combination of these two mentioned methods to take advantage of benefits of either method to solve more complex 3D problems. We also developed two deconvolution techniques to fix the stability problems commonly observed in recovering input motions.

Acknowledgment

The authors would like to acknowledge Dr. Hamed Ebrahimain from the University of Nevada at Reno, and Prof. Asimaki from Caltech for their collaborations in the Bayesian estimation methods. The work presented in this manuscript was funded by the California Geological Survey (Contract No. 1018-563). Any opinions, findings, conclusions or recommendations expressed in this material are those of the authors and do not necessarily reflect the views of the sponsoring agencies.

References

[1] M. R. Gallipoli, M. Mucciarelli, F. Ponzo, M. Dolce, E. D'Alema, and M. Maistrello, "Buildings as a seismic source: Analysis of a release test at Bagnoli, Italy," *Bull. Seismol. Soc. Am.*, 2006.

[2] A. Zerva and V. Zervas, "Spatial variation of seismic ground motions: An overview," *Appl. Mech. Rev.*, vol. 55, no. 3, p. 271, 2002.

[3] J. P. Wolf and A. J. Deeks, Foundation vibration analysis: A strength of materials approach. Butterworth-Heinemann, 2004.

[4] J. P. Stewart, R. B. Seed, and G. L. Fenves, *Empirical evaluation of inertial soil-structure interaction effects*. Pacific Earthquake Engineering Research Center, 1998.

[5] A. L. Pais and E. Kausel, "On rigid foundations subjected to seismic waves," *Earthq. Eng. Struct. Dyn.*, vol. 18, no. 4, pp. 475–489, 1989.

[6] D. G. Lignos and E. Miranda, "Estimation of base motion in instrumented steel buildings using output-only system identification," *Earthq. Eng. Struct. Dyn.*, vol. 43, no. 4, pp. 547–563, 2014.

[7] M. J. Huang and A. F. Shakal, "Structure Instrumentation in the California Strong Motion Instrumentation Program," in *Strong Motion Instrumentation for Civil Engineering Structures*, 2011.

[8] S. F. Ghahari and E. Taciroglu, "IDENTIFICATION OF DYNAMIC FOUNDATION STIFFNESSES AND INPUT MOTIONS FROM STRONG MOTION DATA RECORDED AT CSMIP INSTRUMENTED BUILDINGS," *Conf. Pap. · Oct. 2016 CITATIONS*, 2017.

[9] P. C. Hansen, "Deconvolution and regularization with Toeplitz matrices," *Numerical Algorithms*. 2002.

[10] R. Brincker, L. Zhang, and P. Andersen, "Modal identification of output-only systems using frequency domain decomposition," *Smart Mater. Struct.*, vol. 10, no. 3, pp. 441–445, 2001.

[11] P. Van Overschee and B. De Moor, "Subspace algorithms for the stochastic identification problem," *Automatica*, vol. 29, no. 3, pp. 649–660, 1993.

[12] F. Abazarsa, S. F. Ghahari, F. Nateghi, and E. Taciroglu, "Response-only modal identification of structures using limited sensors," *Struct. Control Heal. Monit.*, vol. 20, no. 6, 2013.

[13] S. F. Ghahari, M. A. Ghannad, and E. Taciroglu, "Blind identification of soil-structure systems," *Soil Dyn. Earthq. Eng.*, vol. 45, 2013.

[14] F. Abazarsa, F. Nateghi, S. F. Ghahari, and E. Taciroglu, "Blind modal identification of non-classically damped systems from free or ambient vibration records," *Earthq. Spectra*, vol. 29, no. 4, 2013.

[15] E. Taciroglu, F. Abazarsa, and S. F. Ghahari, "Response-only identification of torsionally coupled buildings using strong motion data," in *9th International Confernce on Urban Earthquake Engineering/4th Asia Conference on Earthquake Engineering*, 2012.

[16] S. F. Ghahari, F. Abazarsa, M. A. Ghannad, M. Celebi, and E. Taciroglu, "Blind modal identification of structures from spatially sparse seismic response signals," *Struct. Control Heal. Monit.*, vol. 21, no. 5, 2014.

[17] S. F. Ghahari, F. Abazarsa, and E. Taciroglu, "Blind modal identification of non-classically damped structures under non-stationary excitations," *Struct. Control Heal. Monit.*, 2016.

[18] S. F. Ghahari, F. Abazarsa, M. A. Ghannad, and E. Taciroglu, "Response-only modal identification of structures using strong motion data," *Earthq. Eng. Struct. Dyn.*, vol. 42, no. 8, 2013.

[19] S. F. Ghahari, M. A. Ghannad, J. Norman, A. Crewe, F. Abazarsa, and E. Taciroglu, "Considering wave passage effects in blind identification of long-span bridges," in *Conference Proceedings of the Society for Experimental Mechanics Series*, 2013, vol. 5.

[20] F. Abazarsa, F. Nateghi, S. F. Ghahari, and E. Taciroglu, "Extended blind modal identification technique for nonstationary excitations and its verification and validation," *J. Eng. Mech.*, vol. 142, no. 2, 2016.

[21] S. F. Ghahari, F. Abazarsa, O. Avci, M. ??elebi, and E. Taciroglu, "Blind identification of the Millikan Library from earthquake data considering soil-structure interaction," *Struct. Control Heal. Monit.*, vol. 23, no. 4, pp. 684–706, 2016.

[22] E. Taciroglu, M. Çelebi, S. F. Ghahari, and F. Abazarsa, "An investigation of soil-structure interaction effects observed at the MIT green building," *Earthq. Spectra*, vol. 32, no. 4, pp. 2425–2448, 2016.

[23] E. Taciroglu and S. F. Ghahari, "Identification of soil-foundation dynamic stiffness from seismic response signals," in *American Concrete Institute, ACI Special Publication*, 2017, vol. 2017–Janua, no. SP 316.

[24] N. Shirzad-Ghaleroudkhani, M. Mahsuli, S. F. Ghahari, and E. Taciroglu, "Bayesian identification of soil-foundation stiffness of building structures," *Struct. Control Heal. Monit.*, 2017.

[25] E. Taciroglu, S. F. Ghahari, and F. Abazarsa, "Efficient model updating of a multi-story frame and its foundation stiffness from earthquake records using a timoshenko beam model," *Soil Dyn. Earthq. Eng.*, vol. 92, 2017.

[26] H. Ebrahimian, R. Astroza, J. P. Conte, and C. Papadimitriou, "Bayesian optimal estimation for output-only nonlinear system and damage identification of civil structures," *Struct. Control Heal. Monit.*, vol. 25, no. 4, 2018.

[27] E. Ebrahimian, H.;Ghahari, S.F.;Asimaki, D.;Taciroglu, "Estimation of the Soil-Structure Model Parameters for the Millikan Library Building Using a Sequential Bayesian Finite Element Model Updating Technique," *Earthq. Eng.& Struct. Dyn.*, 2019.

[28] S. F. Ghahari, F. Abazarsa, and E. Taciroglu, "Probabilistic blind identification of site effects from ground surface signals," *Bull. Earthq. Eng.*, 2017.

[29] S. F. Ghahari, F. Abazarsa, C. Jeong, A. Kurtulus, and E. Taciroglu, "Blind identification of site effects and bedrock motion from surface response signals," *Soil Dyn. Earthq. Eng.*, vol. 107, pp. 322–331, 2018.

[30] R. Astroza, H. Ebrahimian, Y. Li, and J. P. Conte, "Bayesian nonlinear structural FE model and seismic input identification for damage assessment of civil structures," *Mech. Syst. Signal Process.*, vol. 93, pp. 661–687, 2017.

[31] H. Ebrahimian, R. Astroza, J. P. Conte, and C. Papadimitriou, "Bayesian optimal estimation for output-only nonlinear system and damage identification of civil structures," *Structural Control and Health Monitoring*, 2018.

[32] S. V CSI, "8, 2002. Integrated Finite Element Analysis and Design of Structures Basic Analysis Reference Manual," *Comput. Struct. Inc., Berkeley, California, USA*, 2010.

[33] F. McKenna, "OpenSees: a framework for earthquake engineering simulation," *Comput. Sci. Eng.*, vol. 13, no. 4, pp. 58–66, 2011.

[34] G. Xu, H. Liu, L. Tong, and T. Kailath, "A least-squares approach to blind channel identification," *IEEE Trans. Signal Process.*, vol. 43, no. 12, pp. 2982–2993, 1995.

[35] N. A. Abrahamson, J. F. Schneider, and J. C. Stepp, "Empirical Spatial Coherency Functions for Application to Soil-Structure Interaction Analyses," *Earthq. Spectra*, vol. 7, no. 1, pp. 1–27, 1991.

[36] J. R. Ragazzini and L. A. Zadeh, "The analysis of sampled-data systems," *Trans. Am. Inst. Electr. Eng. Part II Appl. Ind.*, vol. 71, no. 5, pp. 225–234, 1952.

[37] C. P. Hughes and A. Nikeghbali, "The zeros of random polynomials cluster uniformly near the unit circle," *Compos. Math.*, 2008.

[38] A. V Oppenheim, R. W. Schafer, and J. R. Buck, *Discrete Time Signal Processing*, vol. 1999. 1999.

[39] M. Miyoshi and Y. Kaneda, "Inverse Filtering of Room Acoustics," *IEEE Trans. Acoust.*, 1988.

[40] X. Li, S. Gannot, L. Girin, and R. Horaud, "Multisource mint using convolutive transfer function," in *ICASSP, IEEE International Conference on Acoustics, Speech and Signal Processing - Proceedings*, 2018.

[41] Y. Avargel and I. Cohen, "System identification in the short-time fourier transform domain with crossband filtering," *IEEE Trans. Audio, Speech Lang. Process.*, 2007.

[42] J. Bendat and A. Piersol, Engineering applications of correlation and spectral analysis. 1993.

[43] E. Ghahari, S.F., Abazarsa, F., Ebrahimian, H., Taciroglu, "Output-only model updating of adjacent buildings from sparse seismic response records and identification of their common excitation," *Struct. Control Heal. Monit.*, vol. submitted, 2018.

[44] S. Hashemi and J. K. Hammond, "The interpretation of singular values in the inversion of minimum and non-minimum phase systems," *Mech. Syst. Signal Process.*, 1996.

[45] R. Gray, "On the asymptotic eigenvalue distribution of Toeplitz matrices," *IEEE Trans. Inf. Theory*, 1972.

[46] H. Ebrahimian, R. Astroza, J. P. Conte, and R. A. de Callafon, "Nonlinear finite element model updating for damage identification of civil structures using batch Bayesian estimation," *Mech. Syst. Signal Process.*, vol. 84, pp. 194–222, 2017.

[47] S. Haykin, *Kalman Filtering and Neural Networks*, vol. 5, no. 3. 2001.

[48] S. J. Julier and J. K. Uhlmann, "New extension of the Kalman filter to nonlinear systems," in *Signal Processing, Sensor Fusion, and Target Recognition VI*, 1997, vol. 3068, p. 182.

Appendix A: Output-Only Bayesian Estimation

The response of the Finite Element (FE) model of a building at each time step to a multi-directional earthquake excitation can be expressed as a (nonlinear) function of the model parameter vector, $\boldsymbol{\theta}$, and the time history of the base input motions, $\ddot{\boldsymbol{u}}_{1:i}^{g}$, i.e.,

$$\widehat{\boldsymbol{y}}_i = h_i(\boldsymbol{\theta}, \ddot{\boldsymbol{u}}_{1:i}^{g}), \tag{A1}$$

where $h_i(.)$ is the nonlinear response function of the FE model at time step i, encapsulating all the dynamics of the model from time step 1 to i. The measured response vector of the structure, $\boldsymbol{y}_i$, is related to the FE predicted response, $\widehat{\boldsymbol{y}}_i$, as

$$\boldsymbol{v}_i(\boldsymbol{\theta}, \ddot{\boldsymbol{u}}_{1:i}^{g}) = \boldsymbol{y}_i - \widehat{\boldsymbol{y}}_i(\boldsymbol{\theta}, \ddot{\boldsymbol{u}}_{1:i}^{g}), \tag{A2}$$

in which $\boldsymbol{v}_i \in \mathrm{R}^{n_y \times 1}$ is the simulation error vector and accounts for the misfit between the measured and FE predicted response of the structure. The simulation error is ideally modeled as a zero-mean Gaussian white noise vector (i.e., $\boldsymbol{v}_i \sim N(\mathbf{0}, \mathbf{R})$) by neglecting the effects of modeling error [46]. The objective of the estimation problem is to find the estimates of the unknown parameter vector, i.e., $\boldsymbol{\psi}_i = \left[\boldsymbol{\theta}^T, \ddot{\boldsymbol{u}}_{1:i}^{g\ T}\right]^T$, for which the discrepancies between the measured and FE predicted responses are minimized in a probabilistic sense. Since the estimation problem is highly nonlinear, a sequential estimation approach is used in this study to improve estimation efficiency. In this approach, the time domain is divided into successive overlapping time windows, referred to as the estimation windows. The estimation problem is solved at each estimation window to estimate the unknown parameter vector. Assume that the m-th estimation window spans from time step t_1^m to time step t_2^m. Therefore, the unknown parameter vector at this estimation window is defined as $\boldsymbol{\psi}_m = \left[\boldsymbol{\theta}^T, \ddot{\boldsymbol{u}}_{t_1^m:t_2^m}^{g,m\ T}\right]^T$, where $\boldsymbol{\psi}_m \in \mathrm{R}^{(n_{\boldsymbol{\theta}} + t_l \times n_{\ddot{\boldsymbol{u}}^g}) \times 1}$, in which $t_l = t_2^m - t_1^m$ is the estimation window length, and $n_{\ddot{\boldsymbol{u}}^g}$ is the number of unknown components of the base input motions. The unknown parameter vector, $\boldsymbol{\psi}_m$, is estimated using a parameter-only Kalman filtering method. To this end, the unknown parameter vector is modeled as a random vector, the evolution of which is characterized by a Gaussian Markov process – also known as a random walk. Then, a state-space model is set up, in which the state equation governs the evolution of the random parameter vector and the measurement equation corresponds to the discrepancies between the measured and FE predicted structural responses [47], i.e.,

$$\boldsymbol{\psi}_{m,k+1} = \boldsymbol{\psi}_{m,k} + \boldsymbol{\gamma}_{m,k}, \tag{A3}$$

$$\boldsymbol{y}_{t_1^m:t_2^m} = \widehat{\boldsymbol{y}}_{t_1^m:t_2^m,k+1}(\boldsymbol{\psi}_{m,k+1}) + \boldsymbol{v}_{t_1^m:t_2^m,k+1}, \tag{A4}$$

in which $\boldsymbol{\gamma}_{m,k} \sim N(\mathbf{0}, \mathbf{Q})$, $\boldsymbol{v}_{t_1^m:t_2^m,k+1} \sim N(\mathbf{0}, \widetilde{\mathbf{R}})$, where $\widetilde{\mathbf{R}} \in \mathrm{R}^{(t_l \times n_y) \times (t_l \times n_y)}$ is a block diagonal matrix, whose block diagonals are the simulation error covariance matrix $\mathbf{R}$. In Eqs. (A3) and (A4), k denotes the iteration number. As can be observed, the estimation process at each estimation window is iterative, i.e., the mean vector and covariance matrix of the unknown parameter vector is iteratively updated based on the discrepancies between the time histories of the measured and estimated responses.

An Unscented Kalman Filtering (UKF) method is used to update the unknown parameter vector at each iteration. In this method, the nonlinear FE model is evaluated separately at a set of deterministically selected realizations of the unknown parameter vector, which are referred to as the sigma points (SPs) denoted by $\boldsymbol{\vartheta}^j$. The sigma points are selected around the prior mean estimate $\widehat{\boldsymbol{\psi}}^-$. In this study, a scaled Unscented Transformation (UT) based on $2n_{\boldsymbol{\psi}}+1$ sigma points (i.e., $j = 1,2,\ldots,2n_{\boldsymbol{\psi}}+1$) is used, where $n_{\boldsymbol{\psi}}$ denotes the size of the extended parameter vector. The mean and covariance matrix of the FE predicted structural responses, and the cross-covariance matrix of $\boldsymbol{\psi}$ and $\boldsymbol{y}$ are respectively computed using a weighted sampling method as

$$\overline{\boldsymbol{y}} = \sum_{j=1}^{2n_{\boldsymbol{\psi}}+1} W_m^j\, \widehat{\boldsymbol{y}}_i\left(\boldsymbol{\vartheta}^j\right), \tag{A5}$$

$$\widehat{\mathbf{P}}_{\boldsymbol{yy}} = \sum_{j=1}^{2n_{\boldsymbol{\psi}}+1} W_e^j \left[\widehat{\boldsymbol{y}}_i\left(\boldsymbol{\vartheta}^j\right) - \overline{\boldsymbol{y}}\right]\left[\widehat{\boldsymbol{y}}_i\left(\boldsymbol{\vartheta}^j\right) - \overline{\boldsymbol{y}}\right]^T + \mathbf{R}, \tag{A6}$$

$$\widehat{\mathbf{P}}_{\boldsymbol{\psi y}} = \sum_{j=1}^{2n_{\boldsymbol{\psi}}+1} W_e^j \left[\boldsymbol{\vartheta}^j - \widehat{\boldsymbol{\psi}}^-\right]\left[\widehat{\boldsymbol{y}}_i\left(\boldsymbol{\vartheta}^j\right) - \overline{\boldsymbol{y}}\right]^T, \tag{A7}$$

where W_m^j and W_e^j denote weighting coefficients [48]. Now, the UKF prediction-correction procedure can be employed to estimate the posterior parameter mean vector $\widehat{\boldsymbol{\psi}}^+{}_{m,k+1}$ and covariance matrix $\widehat{\mathbf{P}}^+_{\boldsymbol{\psi},m,k+1}$ at each iteration. The identification algorithm is summarized in **Table A1**.

Table A1. Identification algorithm for joint estimation of the model parameters and the FIM time history.

1. Set the estimation window length t_l, and the start and end points of each estimation window.
2. Set the initial mean vector and covariance matrix of the unknown parameter vector as
$$\widehat{\boldsymbol{\psi}}^+{}_0 = \left[\widehat{\boldsymbol{\theta}}_0{}^T, \ddot{\boldsymbol{u}}^{g,0}_{t_1^0:t_2^0}{}^T\right]^T, \text{ and } \mathbf{P}^+_{\boldsymbol{\psi},0} = \begin{bmatrix} \widehat{\mathbf{P}}_{\boldsymbol{\theta\theta},0} & \mathbf{0} \\ \mathbf{0} & \widehat{\mathbf{P}}_{\ddot{\boldsymbol{u}}^{g,0}} \end{bmatrix}.$$
3. Define the process noise covariance matrix $\mathbf{Q}$ and the simulation error covariance matrix $\mathbf{R}$. Set up matrix $\widetilde{\mathbf{R}}$.
4. For the m-th estimation window:
   - 4.1. Retrieve the posterior estimates of the mean vector and covariance matrix of the unknown parameter vector from the last estimation window (i.e., $\widehat{\boldsymbol{\psi}}^+{}_{m-1}$, and $\mathbf{P}^+_{\boldsymbol{\psi},m-1}$). Set up $\widehat{\boldsymbol{\psi}}^+{}_{m,0}$ and $\mathbf{P}^+_{\boldsymbol{\psi},m,0}$ based on $\hat{\boldsymbol{\psi}}^+_{\boldsymbol{m}-1}$ and $\mathbf{P}^+_{\boldsymbol{\psi},m-1}$.
   - 4.2. Iterate (k = 1, 2, …):
     - a. Set $\widehat{\boldsymbol{\psi}}^-{}_{m,\mathrm{k}+1} = \widehat{\boldsymbol{\psi}}^+{}_{m,\mathrm{k}}$, $\mathbf{P}^-_{\boldsymbol{\psi},m,k+1} = \mathbf{P}^+_{\boldsymbol{\psi},m,k} + \mathbf{Q}$.
     - b. Generate sigma points. Run the FE model for $(2n_{\boldsymbol{\psi}}+1)$ sigma points. Derive $\overline{\boldsymbol{y}}$, $\widehat{\mathbf{P}}_{\boldsymbol{yy}}$, and $\widehat{\mathbf{P}}_{\boldsymbol{\psi y}}$ using Eqs. (A5)-(A7).
     - c. Compute the Kalman gain matrix: $\mathbf{K} = \widehat{\mathbf{P}}_{\boldsymbol{\psi y}}\left(\widehat{\mathbf{P}}_{\boldsymbol{yy}}\right)^{-1}$.
     - d. Find the corrected estimates of the mean vector and covariance matrix of the unknown parameter vector:
       $\widehat{\boldsymbol{\psi}}^+{}_{m,\mathrm{k}+1} = \widehat{\boldsymbol{\psi}}^-{}_{m,\mathrm{k}+1} + \mathbf{K}\left(\boldsymbol{y}_{t_1^m:t_2^m} - \overline{\boldsymbol{y}}\right)$, $\mathbf{P}^+_{\boldsymbol{\psi},m,k+1} = \mathbf{P}^-_{\boldsymbol{\psi},m,k+1} - \mathbf{K}\left(\widehat{\mathbf{P}}_{\boldsymbol{yy}} + \widetilde{\mathbf{R}}\right)\mathbf{K}^T$.
     - e. Check for convergence: if $\left|\widehat{\boldsymbol{\psi}}^+{}_{m,k+1} - \widehat{\boldsymbol{\psi}}^+{}_{m,k}\right| < 0.02 \times \widehat{\boldsymbol{\psi}}^+{}_{m,k-1}$ or $k+1 > 10$, then move to the next estimation window ($m = m + 1$, go to step 4); otherwise, iterate again at the current estimation window ($k = k + 1$, go to step 4.2).